Journal of Luminescence 251 (2022) 119135

Contents lists available at ScienceDirect

Journal of Luminescence

journal homepage: www.elsevier.com/locate/jlumin

Full Length Article

Mixed ionic–electronic effect on up–conversion in Er^{3+}/V^{4+} co–doped Na_2O–CaO–B_2O_3 glasses with enhanced red emission☆,☆☆

S.N. Mohamed [a,*], E.S. Sazali [b], A.K. Yahya [a]

[a] Faculty of Applied Sciences, Universiti Teknologi MARA, 40450 Shah Alam, Selangor, Malaysia
[b] Advanced Optical Materials Research Groups, Department of Physics, Faculty of Science, Universiti Teknologi Malaysia, 81310 Skudai, Johor, Malaysia

ARTICLE INFO

Keywords:
Borate glass
Judd–ofelt analysis
Up–conversion
Elastic properties
Energy transfer

ABSTRACT

Optical absorption and emission properties of $20Na_2O$–20CaO–$(59 - x)B_2O_3$–xV_2O_5–$1Er_2O_3$ ($x = 0 - 2.5$ mol%) (Series A) and $20Na_2O$–20CaO–$(58.5 - y)B_2O_3$–$1.5V_2O_5$–yEr_2O_3 ($y = 0 - 3.0$ mol%) (Series B) glass systems were examined to elucidate the effect of Er_2O_3 co–doping with V_2O_5 in the mixed ionic–electronic (MIE) glasses. The absorption spectra of both glass series exhibited 10 significant bands, which corresponded to the *f–f* transition of Er^{3+} ions with an additional weak absorption band attributed to V^{4+} energy transition. The up–conversion PL spectra for the glasses under 779 nm excitation displayed 3 emissions bands centered at 518, 556 and 647 nm due to the emission from the energy levels of Er^{3+}. The enhanced emission at 647 nm (red region) that corresponded to the $^4F_{9/2} \rightarrow {}^4I_{15/2}$ of the Er^{3+} transition for all glasses was suggested due to energy transfer from V^{4+} to Er^{3+} ions. For Series A, the variation of oscillator strength (f_{exp}) and Judd–Ofelt parameters ($\Omega_{2,4,6}$) showed almost similar trend, which exhibit a maximum at $x = 0.5$ mol% V_2O_5. PL intensity was highest for sample $x = 0.5$ mol% but abruptly drops to the minimum at $x = 1.5$ mol%. The decrease in PL was possibly influenced by the MIE effect. Meanwhile, for Series B glasses, general decrease was observed in f_{exp} and Judd–Ofelt parameters except for Ω_6 upon Er_2O_3 addition. The PL intensity increased and reached a maximum at $y = 2.0$ mol% before subsequently decreased with further addition of Er_2O_3 ($y = 3.0$ mol%) due to concentration quenching.

1. Introduction

Borovanadate glasses consisting of mixed network formers, namely B_2O_3 and V_2O_5 in the glass composition have attracted considerable interest because of their notable structural and physical properties [1,2]. The incorporation of two dissimilar host glasses have shown non– linear variation of certain properties such as conductivity and glass transition temperature, which termed as the mixed glass former effect (MGFE) [3]. B_2O_3 is a well–known host glass that displays unique physical properties, such as the borate anomaly when alkali or alkaline– earth metal oxide is introduced to the glasses as a modifier. The borate anomaly was explained by considering the transformation of three– to four–fold coordinated boron during the initial addition of modifier oxides before non–bridging oxygens (NBO) were created at higher modifier contents. Meanwhile, V_2O_5 is a conditional glass that can form a glass through the addition of other components under conventional quenching conditions. Introduction of V_2O_5 into alkali borate glasses exhibits a mixed ionic–electronic (MIE) effect, which involves the interaction between ionic and electronic carriers. The signature of the MIE effect has been demonstrated in electrical conductivity studies on the conductivity minimum when one type of carrier is replaced partially by another [4,5].

Several suggestions have been proposed to explain the MIE–related conductivity minimum in terms of ion–polaron interactions or the reduction of transition metal oxide concentrations [6]. In our recent work [7], we reported the MIE effect on DC conductivity in borovanadate glasses, in which the effect was explained in contrast on the basis of ionic blo8cking attributed to V^{4+} ions outside of the glass network. As such, the MIE effect has only been partially understood at present. For MIE glasses, non–linear variations have been observed in other glass properties, such as in elastic moduli [7], dielectric constant [8] and internal friction [9]. These variations have been presumed due to the MIE effect. Therefore, it is becoming increasingly important to understand the other glass properties apart from the conductivity properties, such as the absorption and emission properties, because

☆ The paper presents original work not previously published in similar form and not currently under consideration by another Journal.
☆☆ The authors followed ethics guidelines.
* Corresponding author.
E-mail address: syafawati@uitm.edu.my (S.N. Mohamed).

https://doi.org/10.1016/j.jlumin.2022.119135
Received 24 March 2021; Received in revised form 4 July 2022; Accepted 11 July 2022
Available online 19 July 2022

these characteristics might also reflect the MIE effect.

Conversely, rare earth (RE) doped glasses have received considerable attention in photonic applications because of their interesting optical properties. The use of luminescence glass as an active medium in solid–state laser is a promising alternative to compensate classical luminescent host. Emission from glass materials can be achieved by doping REs, such as Er^{3+} ions, into the glass host. Several researchers have studied Er^{3+} doped oxide glasses through photoluminescence (PL) spectroscopy because of their favorable green and red emissions [10,11]. Er^{3+} doped glasses require a high concentration of Er^{3+} ions to achieve a strong emission [12]. However, a high doping level of Er^{3+} ions may cause clustering, which leads to luminescence quenching and large non–radiative losses [13]. Several practical approaches have been proposed to improve the emission properties of RE–doped glass co–doped with various REs [14,15] or transition metal ions [16,17]. Previous reports confirmed that the emission intensity of Er^{3+} co–doped with other RE ions is stronger than that of single Er^{3+} doped glasses. Co–doped systems are investigated continually because their emission properties depend on the host composition. Spectroscopic studies involving transition metal ions have also attracted reasonable interest because of the existence of the partially filled d orbital. Their emission spectra arise from the *d–d* transition and exhibit considerably broader spectrum lines than the spectra of RE ions. As mentioned above, vanadium ions exist in two valence states and different structural units, thus offering varying environmental conditions for RE ions in the glass network which can enhance the PL behavior of RE ions and render them suitable for optical applications. Spectroscopic studies have shown that an additional band appears in the emission spectra of $40Na_2O–54SiO_2–(5 – x)ZrO_2–1Ho_2O_3–xV_2O_5$, which suggested that vanadium ions participated in the radiative transitions within the glass network [17]. The presence of V_2O_5 in a host matrix offers a convenient environment for hosting the RE ions to produce efficient luminescence with low phonon losses. Thus, the local environment of RE ions in the oxide glass system is expected to depend not only on the composition of the host matrix but also on the concentration of V_2O_5, thereby producing different crystal field strengths. Consequently, varied optical and spectral properties are expected. Although several works have been reported on the emission properties of V_2O_5–doped RE glasses, further investigations are necessary to elucidate the role of V_2O_5 in modifying the luminescence characteristics of activator ions, especially in Er^{3+} doped glasses. As such, this compound has become an interesting material for potential application in up–conversion lasers.

Interestingly, the effects of mixed alkali on optical absorption and emission have been previously investigated in Sm^{3+}– and Dy^{3+}–doped $69.5B_2O_3–xLiCl–(30 – x)NaCl–0.5R_2O_3$ (where R = Sm and Dy and x = 5, 10, 15, 20 and 25) glasses [18] where results showed significant maximum emission transition at x = 10 mol% and at x = 20 mol% in Sm^{3+} and Dy^{3+} ion–doped lithium–sodium, respectively. The finding indicates that the mixed alkali influences the emission properties. To the best of our knowledge, the optical spectra of RE doped host composition from MIE glass, in contrast to those of mixed alkali glasses, remain unexplored. In our previous work, MIE carriers also influenced the optical properties of $20Na_2O–20CaO–(60 – x)B_2O_3–xV_2O_5$ glasses [7], where the optical energy band gap and the refractive index exhibit minimum and maximum values, respectively, at x = 1.5 mol% of V_2O_5 content. The observed anomalies in both optical energy band gap and refractive index coincided with the conductivity anomaly region, suggesting that the MIE may also affect both properties. As an extension, it would be of interest to study the effect of Er_2O_3 activator ions added to the $Na_2O–CaO–B_2O_3–V_2O_5$ MIE glass system to look into possible of Er^{3+}–vanadium ions interaction and energy transfer behavior in the MIE conductivity anomaly region. It is hope that this study will contribute to better understanding of energy transfer. Moreover, to our knowledge, both optical studies of absorption and emission properties have not been reported for Er^{3+}/V^{4+} co– doped $Na_2O–CaO–B_2O_3–V_2O_5$ MIE glass system.

In this work, we investigated the effect of co–doped Er_2O_3:V_2O_5 on the structural, optical absorption and emission properties of two different series of glasses with compositions of $20Na_2O–20CaO–(59 – x)B_2O_3$:$xV_2O_5–1Er_2O_3$ and $20Na_2O–20CaO–(58.5 – y)B_2O_3$:$1.5V_2O_5–yEr_2O_3$ glass systems by using FTIR, UV–vis–NIR measurement, and photoluminescence (PL) spectroscopy. In addition, further analysis involving the oscillator strength by using Judd–Ofelt theory and energy transfer mechanism was performed based on the PL spectra. The knowledge of oscillator strength and energy transfer as a function of composition is important in understanding the absorption and emission properties in the conductivity anomaly region of MIE glass systems.

2. Experimental details

2.1. Preparation of samples

Glass samples with chemical glass compositions of $20Na_2O–20CaO–(59 – x)B_2O_3–xV_2O_5–1Er_2O_3$ (x = 0, 0.5, 1.0, 1.5, 2.0 and 2.5 mol%) (Series A) and $20Na_2O–20CaO–(58.5 – y)B_2O_3–1.5V_2O_5–yEr_2O_3$ (y = 0, 1.0, 2.0 and 3.0 mol%) (Series B) were synthesized using melt–quenching method. Details of the chemical composition of the glasses are shown in Table 1. The glasses were prepared using analytical reagent grade 99.99%, sodium carbonates (Na_2CO_3), calcium carbonate ($CaCO_3$), vanadium oxide (V_2O_5), erbium oxide (Er_2O_3) and boron oxide (B_2O_3). The Er_2O_3–free quaternary glasses with formula $20Na_2O–20CaO–(60 – x)B_2O_3–xV_2O_5$ have been prepared previously [7]. The raw materials were carefully weighed using electronic balance, well mixed and ground continuously by using an agate mortar and pestle set for 1 h until a fine homogenous powder was achieved. The mixture was then placed in an alumina crucible and melted for 1 h in a box furnace at 1100 °C. The melt samples were rapidly quenched in a stainless steel mould and annealed at 300 °C for 5 h to remove the thermal strain in the glasses. The samples were polished using sand paper for optical absorption, PL and ultrasonic velocity measurements. The samples were crushed into powder form for X–ray diffraction (XRD) and Fourier transform infrared (FTIR) absorption measurements.

2.2. Characterization of glasses

XRD studies were carried out in the X'Pert Pro Panalytical diffractometer to confirm glassy nature of the prepared samples. The density (ρ) of the glass samples was determined at room temperature by Archimedes principle with xylene as the immersion medium through the following equation:

$$\rho = \left(\frac{w}{w - w_b}\right)\rho_b \quad (1)$$

where w is the glass sample weights in air, w_b is the glass sample weights in liquid xylene and ρ_b is the density of xylene (0.865 g mL^{-1}). The molar volume (V_a) was obtained using the following relation:

Table 1
Chemical compositions of Er_2O_3 doped $Na_2O–CaO–B_2O_3–V_2O_5$ glasses.

Glass ID	Glass composition (mol%)				
	Na_2O	CaO	B_2O_3	V_2O_5	Er_2O_3
Series A $[20Na_2O–20CaO–(59 – x)B_2O_3–xV_2O_5–1Er_2O_3]$ (x = 0–2.5 mol%)					
V0	20.0	20.0	59.0	0	1.0
V0.5	20.0	20.0	58.5	0.5	1.0
V1.0	20.0	20.0	58.0	1.0	1.0
V1.5	20.0	20.0	57.5	1.5	1.0
V2.0	20.0	20.0	57.0	2.0	1.0
V2.5	20.0	20.0	56.5	2.5	1.0
Series B $[20Na_2O–20CaO–(58.5 – y)B_2O_3–1.5V_2O_5–yEr_2O_3]$ (y = 0–3.0 mol%)					
E0 [7]	20.0	20.0	58.5	1.5	0
E1.0	20.0	20.0	57.5	1.5	1.0
E2.0	20.0	20.0	56.5	1.5	2.0
E3.0	20.0	20.0	55.5	1.5	3.0

$$V_a = \frac{M}{\rho} \quad (2)$$

where M is the molar mass of the glass.

The IR absorption spectra of the glass powder samples were recorded using a PerkinElmer model Spectrum One FTIR spectrometer to investigate the functional group within the range of 400–1600 cm^{-1}. Each powder sample was mixed with KBr at a fixed ratio of 1:80 and pressed into a pellet with the use of a hand press.

The ultrasonic wave velocities were carried out at room temperature at a frequency of 5 MHz in both longitudinal and shear modes by applying the pulse–echo technique using the RITEC RAM–500–M6 high–performance ultrasonic system. The elastic moduli and the related quantities were calculated using the following equations [19]:

Longitudinal modulus,

$$C_L = v_L^2 \rho \quad (3)$$

shear modulus,

$$\mu = v_S^2 \rho \quad (4)$$

Young's modulus,

$$Y = \frac{\mu(3C_L - 4\mu)}{C_L - \mu} \quad (5)$$

Debye temperature,

$$\theta_D = \left(\frac{h}{k_B}\right)\left(\frac{3PN_A}{4\pi V_a}\right)^{1/3} v_m \quad (6)$$

where ν_L is the longitudinal velocity, ν_S is the shear velocity, h is Planck's constant, k_B is Boltzmann's constant, N_A is Avogadro's number, ν_m is the mean sound velocity, V_a is the molar volume and P is the number of the atoms in the chemical formula.

The absorption spectra were obtained with a PerkinElmer UV–vis–NIR spectrophotometer in the range of 200–1600 nm at room temperature. The room–temperature up–conversion emission and time decay measurements were conducted using a PerkinElmer LS–55 luminescence spectrometer with a pulsed xenon lamp as the excitation source.

3. Results

3.1. XRD and physical properties

The XRD patterns for both glasses in Series A and Series B exhibited broad humps with the complete absence of any sharp peak, as shown in Fig. 1. In this work, the absence of sharp peak in the XRD patterns implied that a crystalline phase and a long–range atomic arrangement did not exist in the samples [20], thereby confirming the amorphous nature of all glass samples. For Series A glasses, the observed broad hump at the scattering angle range of 20°–40° [Fig. 1 (a)] indicated that the mid–range structure failed to crystallize. The intensity of the XRD hump of the glasses was strong at $0 \leq x < 1.5$ mol% and weakened at $x \geq 1.5$ mol%, indicating that the mid–range structure was reduced in the glass samples with the addition of V_2O_5. Moreover, the position of the maximum 2θ of each sample shifted to higher 2θ values at $0 \leq x < 1.5$ mol% and then shifted to lower 2θ at $x > 1.5$ mol%. As previously reported in other glass systems [21–23], a shift towards higher 2θ values indicates a shortening of the network bond length. Therefore, the changes in the 2θ maximum position of the amorphous peak in the present glasses suggest that structural changes occurred in the glasses that made the glass more compact. By contrast, Fig. 1 (b) shows two broad humps for Series B glasses at the scattering angle range of 20°–40° and 40°–60° with the substitution of Er_2O_3 in the glass system, indicating that the glasses were composed of two mid–range phases. The intensity of the hump displayed a non–linear variation trend where it

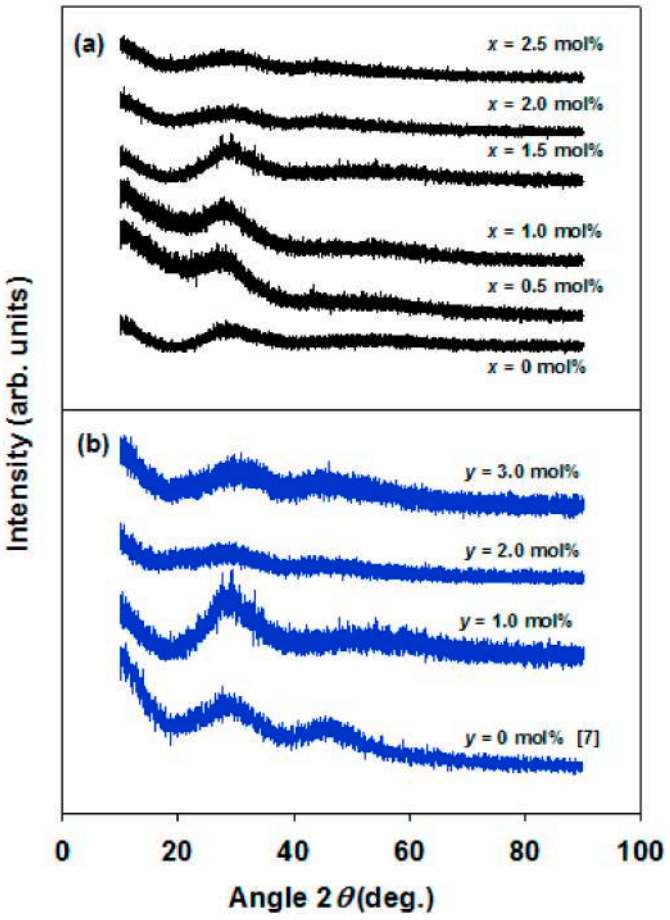

Fig. 1. The XRD patterns of (a) $20Na_2O–20CaO–(59 – x)B_2O_3–xV_2O_5–1Er_2O_3$ (x = 0–2.5 mol%) and (b) $20Na_2O–20CaO–(58.5 – y)B_2O_3–1.5V_2O_5–yEr_2O_3$ (y = 0–3.0 mol%) glass samples.

increases at $y \leq 1.0$ mol%, decreasing at $y = 2.0$ mol%, and then increasing again at $y = 3.0$ mol%. The decrease in the intensity of the hump indicates that the mid–range structure of the glass was reduced, such that a less compact network was expected for the glass at $y = 2.0$ mol%.

Table 2 lists the physical properties for both series of glasses, including the molar volume (V_a), Er^{3+} ion concentration (N), polaron radius (r_p) and inter–ionic distance (r_i) of the glass samples. All of these physical properties were determined based on the measured density (ρ) and average molar mass (M) values of the samples by using following

Table 2
Value of density (ρ), molar volume (V_a), Er^{3+} ion concentration (N), polaron radius (r_p) and inter–ionic distance (r_i) of prepared glass samples.

Sample	ρ (kg m^{-3}) ±2	V_a (m^3 mol^{-1}) ±0.061	N x 10^{22} (ions cm^{-3}) ±0.01	r_p x 10^{-8} (m) ±0.01	r_i x 10^{-8} (m)
Series A [$20Na_2O–20CaO–(59 – x)B_2O_3$: $xV_2O_5–1Er_2O_3$] (x = 0–2.5 mol%)					
V0	2533	2.70	2.23	1.43	3.55
V0.5	2542	2.72	2.22	1.43	3.56
V1.0	2555	2.73	2.21	1.44	3.56
V1.5	2559	2.75	2.20	1.44	3.57
V2.0	2554	2.77	2.17	1.44	3.58
V2.5	2560	2.79	2.16	1.45	3.59
Series B [$20Na_2O–20CaO–(58.5 – y)B_2O_3$:$1.5V_2O_5–yEr_2O_3$] ($y$ = 1.0–3.0 mol%)					
E0 [7]	2547	2.63	0	0	0
E1.0	2559	2.74	2.20	1.44	3.57
E2.0	2629	2.78	4.32	1.15	2.85
E3.0	2737	2.79	6.47	1.00	2.49

equations [13]:

$$N = \frac{mol\%\ \ ofdopant\ \ \mathrm{x}\ \ \rho\ \ \mathrm{x}\ \ N_A}{M} \tag{7}$$

$$r_i = \left(\frac{1}{N}\right)^{\frac{1}{3}} \tag{8}$$

$$r_p = \frac{1}{2}\left(\frac{\pi}{6N}\right)^{\frac{1}{3}} \tag{9}$$

where N_A is the Avogadro number. The Er^{3+} ion concentration gradually decreased in Series A glass, whereas the polaron radius and inter–ionic distance of Er^{3+} ions slightly remained constant with increasing V_2O_5. However, the addition of Er_2O_3 in Series B increased the Er^{3+} ion concentration as expected and greatly reduced the polaron radius and inter–ionic distance of the glass.

Fig. 2 (a) shows the variation of density (ρ) and molar volume (V_a) of Series A glasses. The ρ increased with addition of V_2O_5 except for composition at $x = 2.0$ mol%, for which a sudden drop was observed. The corresponding V_a of this glass increased throughout the compositions range ($x = 0$–2.5 mol%), with a small increase between $x = 0.5$ mol % and $x = 1.0$ mol% before a slightly greater increase at $x > 1.0$ mol%. Fig. 2 (b) shows that ρ increased as the Er_2O_3 content was increased in Series B glasses. By contrast, V_a of Series B glasses increased rapidly from $y = 0$ mol% to $y = 2.0$ mol% (percentage of change: 5.83%), followed by a moderate increase at $y = 3.0$ mol% (0.16%) with gradual substitution of B_2O_3 by Er_2O_3. In addition, the value of ρ due to addition of Er_2O_3 produced more significant changes than those brought about by the substitution of V_2O_5 into the borate glass, as shown in Table 2.

3.2. Infrared spectra

Fig. 3 (a) and **3 (b)** show the FTIR spectra for Series A and Series B,

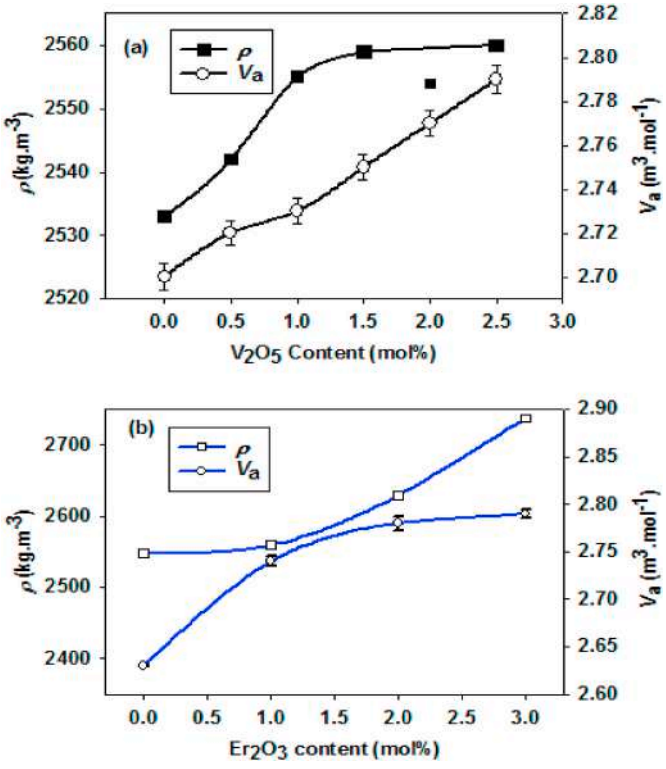

Fig. 2. The density (ρ) and molar volume (V_a) of (a) $20Na_2O$–$20CaO$–$(59 - x)$ B_2O_3–xV_2O_5– $1Er_2O_3$ (x = 0–2.5 mol%) and (b) $20Na_2O$–$20CaO$–$(58.5 - y)$ B_2O_3–$1.5V_2O_5$–yEr_2O_3 (y = 0–3.0 mol%) glass samples.

respectively and the example of deconvolution of the spectrum for sample $x = 1.0$ mol% is given in Fig. 3 (c). The spectra in Fig. 3 (a) is characterized by five main absorption bands i.e. at 512–569, 719–766, 901–1013, 1061–1259 and 1340–1524 cm^{-1}. The band at 512–569 cm^{-1} was assigned to the borate deformation modes, such as the in–plane bending of B–O triangles [24]. From the V_2O_5–free sample V0 ($x = 0$ mol%), two bands were observed, which belong to vibrations of B–O–B bending in BO_3 (672 cm^{-1}) and stretching B–O–B bonds in BO_4 units from triborate, tetraborate and pentaborate groups (847 cm^{-1}), respectively, indicating the existence of both the four-coordinated and three-coordinated boron in the glass structure [25]. With the addition of V_2O_5, IR band appeared at 746 cm^{-1} originating from bending vibrations V–O–V of VO_4 tetrahedral group [26]. The band shifts at about 719–766 cm^{-1} with increasing V_2O_5 content and the relative area of the band increased throughout the series of glass systems. The shift indicates that V–O–V bonding has been gradually substituted by V–O–B bonding, which could be taken as evidence that VO_4 tetrahedra have formed linkages with BO_4 tetrahedra or BO_3 triangles. Bhargava et al. studied the structure of V_2O_5–P_2O_5 glass system and assigned the IR band at 762 cm^{-1} to the vibration of the V–O bond connected to phosphate groups [27]. IR bands in V_2O_5–TeO_2 glass system was found at 730–810 cm^{-1} which is referred to as the vibration of V–O–Te [28]. In our glasses, the IR bands at around 719–766 cm^{-1} are suggested to be related to the vibration of the V–O bond present in the VO_4 connecting borate groups (V–O–B). Besides, the band at 901–1013 cm^{-1} is attributed to the stretching vibrations of B–O bonds in BO_4 units [25]. In the region of vibrations of BO_4 units, a band originating from the stretching vibrations of the isolated V═O group in VO_5 trigonal bipyramids (tbp) unit is also expected to overlap in the same region. The characteristic vibrations of the isolated vanadium–oxygen bonds in the IR spectrum were in the range of 900–1020 cm^{-1} [8,26]. As a result, we may assume the observed band in the region is due to the vibration of isolated V═O group or B–O–V bridging bonds. The relative area of the overlapping BO_4/V═O band increased at $x \leq 1.0$ mol% and decreased at $x > 1.0$ mol % with the peak shifted to a lower wavenumber. Furthermore, the bands at 1061–1259 and 1340–1524 cm^{-1} were assigned to the stretching vibrations of non–bridging $B–O^-$ bonds from the BO_3 units from metaborate, pyroborate and orthoborate groups [29]. The relative areas of the bands increased for all the range of x values between 0.5 mol% and 2.5 mol%.

Fig. 3 (b) shows five majors IR absorption bands were detected with the addition of Er_2O_3 content. The band at 500–569 cm^{-1} was assigned to the borate deformation modes, whereas the band at 702–737 cm^{-1} was assigned to the combine vibrations of V–O bending in VO_4 tetrahedral and B–O bending in borate groups. The band lying at 896–1018 cm^{-1} is attributed to the same assignment in Series A because of overlapping BO_4/V═O band. The bands around 1094–1201 and 1367–194 cm^{-1} are due to the stretching vibrations of non–bridging $B–O^-$ bonds from the BO_3 units from metaborate, pyroborate and orthoborate groups. The relative area for the BO_3 assigned band initially increased with Er_2O_3 at $y \leq 2.0$ mol% before decreasing for $y = 3.0$ mol%. Conversely, the relative area of the BO_4/V═O assigned band shows initially decreased at $y \leq 2.0$ mol% but increased at $y = 3.0$ mol%.

3.3. Optical properties

3.3.1. Optical absorption spectra, refractive index and oscillator strengths

The UV–Vis–NIR absorption spectra under various V_2O_5 (Fig. 4) and Er_2O_3 (Fig. 5) contents show two general absorption regions. First one is the absorption edge which occurs near ultraviolet region while second one is absorption bands observed in the visible region. When Er_2O_3 is doped to the both series glasses, the absorption spectrum reveal ten prominent bands centered at 1531, 977, 799, 651, 544, 521, 488, 451, 443 and 407 nm; these bands were observed due to electrostatic and spin orbit interactions of the 4*f*–transitions of Er^{3+} from ground state $^4I_{15/2}$ to the various excited states of $^4I_{13/2}$,$^4I_{11/2}$, $^4I_{9/2}$, $^4F_{9/2}$,$^4S_{3/2}$, $^2H_{11/2}$, $^4F_{7/2}$,

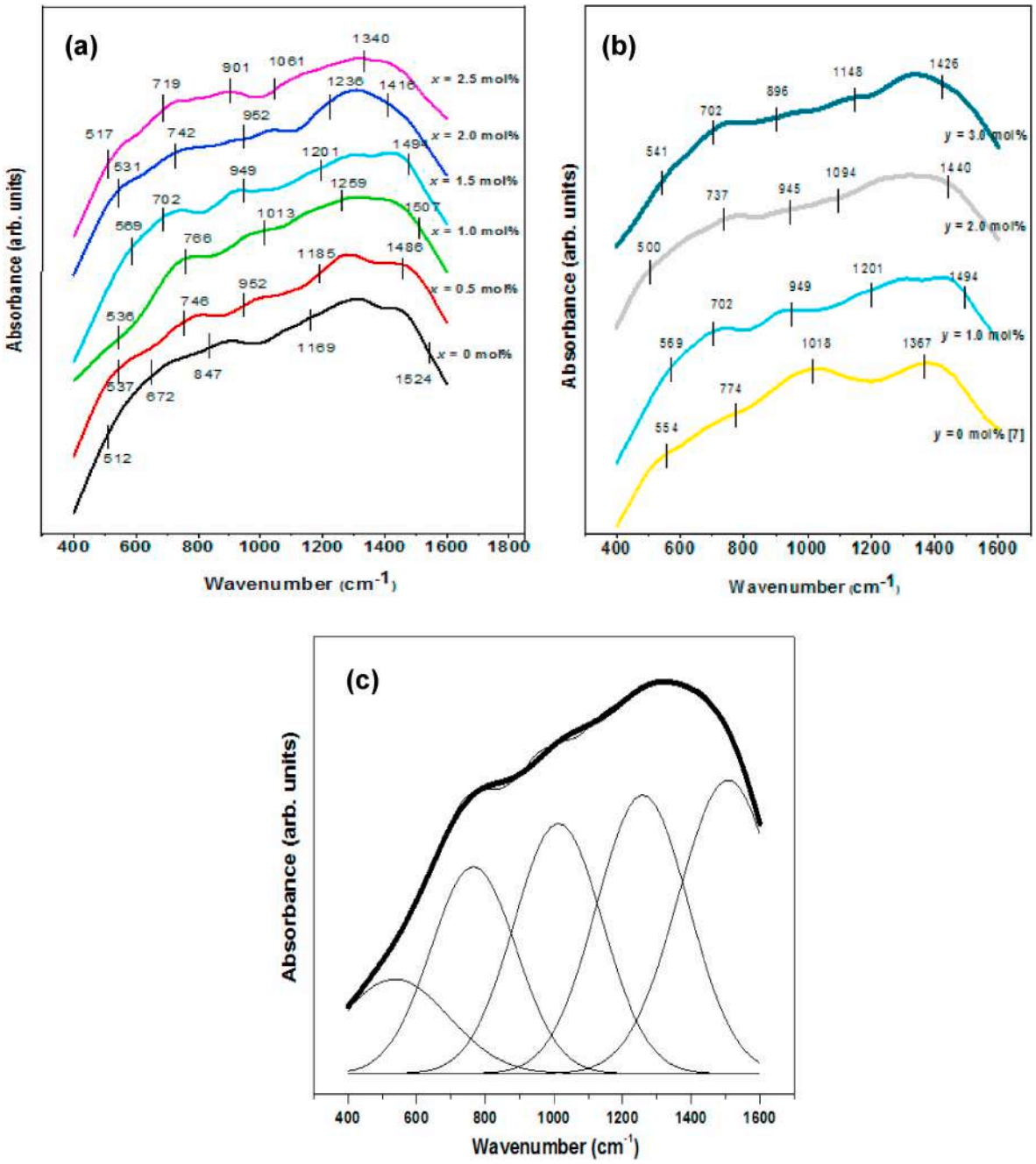

Fig. 3. FTIR spectra of (a) $20Na_2O–20CaO–(59 – x)B_2O_3–xV_2O_5–1Er_2O_3$ (x = 0–2.5 mol%) and (b) $20Na_2O–20CaO–(58.5 – y)B_2O_3–1.5V_2O_5–yEr_2O_3$ (y = 0–3.0 mol %) glass samples. (c) Band deconvolution for $20Na_2O–20CaO–58B_2O_3–1V_2O_5–1Er_2O_3$ glass.

$^4F_{5/2}$, $^4F_{3/2}$ and $^2H_{9/2}$, respectively. The assignments of these bands have been made on the basis of the reported energy level of Er^{3+} ions in different glass systems [24–26]. All the above– mentioned absorption bands for both series of glasses appeared at same positions regardless of composition change. In Series A, a closer look at Fig. 4 reveals that with the addition of V_2O_5, an additional band is observed in the spectral range 580–595 nm for samples x = 0.5–2.5 mol% due to the 3 d^1 V^{4+} absorption transition from $^2B_2$ to $^2B_1$ state [32–34]. No such absorption bands are detected for the V_2O_5–free sample V0 (x = 0 mol%). The results are clearly shown in the insets (a) and (b) of Fig. 4 which show the enlarged view of the area marked by the dashed line. Since the concentration of V_2O_5 in the glass samples was relatively small (0–2.5 mol %), the absorption band related to the V^{4+} ion was weak. In Series B, the Er_2O_3–free sample E0 (y = 0 mol%) was also examined to confirm the observed weak band in the spectra is contributed by V_2O_5. The inset of Fig. 5 displays a relatively small kink at ~590 nm as a result of the existence of tetravalent states of V^{4+}.

From the observed edge, the optical band gap (E_{opt}) and Urbach energy (E_U) for both series of glasses are obtained from the UV–vis absorption spectra. The absorption coefficient (α) near the absorption edge, which is related to transmitted light out of a glass sample with thickness, d can be calculated according to Beer–Lambert law [37]:

$$I_t = I_o exp^{(\alpha d)} \quad (10)$$

where I_o and I_t are the incident and transmitted photon intensities. The E_{opt} was obtained by drawing a Tauc plot through the Davis and Mott relation, with the parameter α given by Ref. [23]:

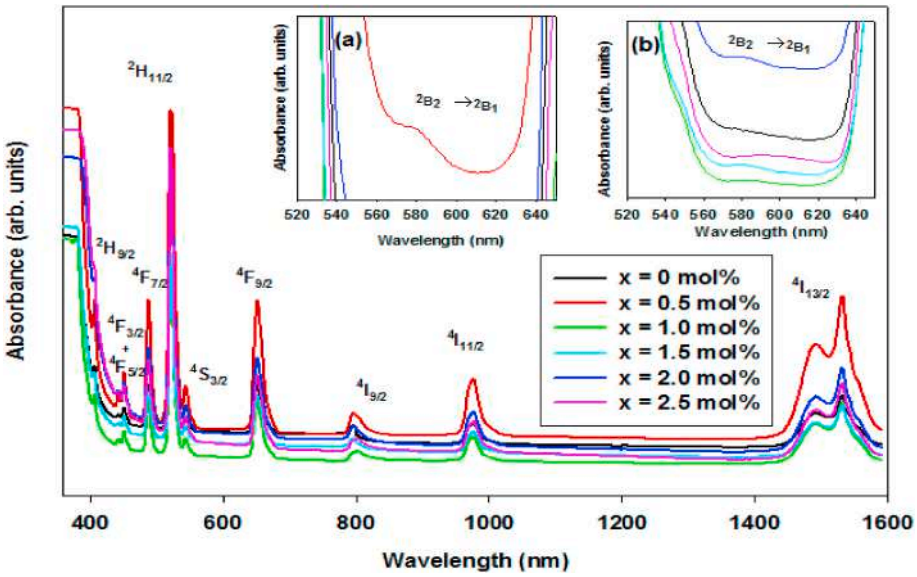

Fig. 4. Optical absorption spectra of $20Na_2O–20CaO–(59 – x)B_2O_3–xV_2O_5–1Er_2O_3$ (x = 0–2.5 mol%) glass samples. Insets are enlargements showing band of V^{4+} for samples (a) x = 0.5 mol% V_2O_5 and (b) x = 0, 1.0, 1.5, 2.0 and 2.5 mol% V_2O_5.

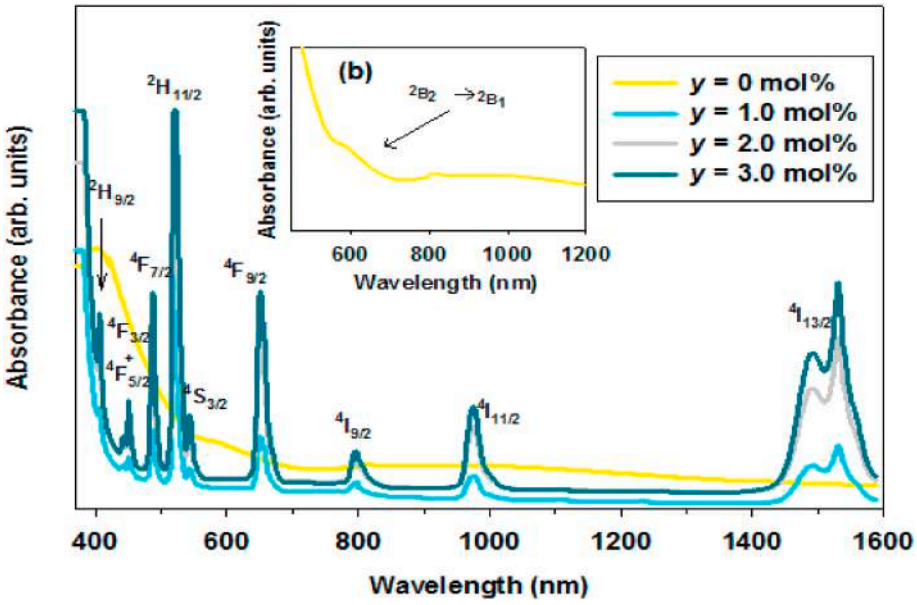

Fig. 5. Optical absorption spectra of $20Na_2O–20CaO–(58.5 – y)B_2O_3–1.5V_2O_5–yEr_2O_3$ (y = 0–3.0 mol%) glass samples. Inset shows peak at 590 nm in detail for $20Na_2O–20CaO–58.5B_2O_3–1.5V_2O_5$ glass sample without Er_2O_3 (y = 0 mol%).

$$\alpha(\omega) = \frac{A(h\nu - E_{opt})^s}{h\nu} \tag{11}$$

where A is a constant, h is Planck's constant, ν is the photon frequency. For the amorphous material, indirect transitions are valid where the value of s is 2 [20]. The E_{opt} values for both glasses are tabulated in Table 3. The Tauc's plots for all glasses are shown in Fig. 6 where values of E_{opt} are estimated from by extrapolating the straight–line part of the curves to the x–axis where $(\alpha h\nu)^{1/2} = 0$. The E_{opt} values that lie in the range of 2.97 eV–2.66 eV for Series A [(Fig. 7 (a)] increase with V_2O_5 content at 0 mol% $\leq x \leq$ 0.5 mol% and begins to decrease beyond x = 0.5 mol%. For Series B, Fig. 7 (b) reveals that E_{opt} rises from 2.40 eV (y = 0 mol%) to 2.93 eV (y = 2.0 mol%) with increasing Er_2O_3 content and diminishes to 2.89 eV for glass at y = 3.0 mol%.

Meanwhile, the width of tail (Urbach energy, E_U) in the forbidden gap can be calculated using this Urbach Law:

$$\alpha(\nu) = C\exp\left(\frac{h\nu}{E_u}\right) \tag{12}$$

where C is a constant. The values of E_U presented in Table 3 were determined by taking the reciprocals of the slope of the linear portion of $\ln(\alpha)$ versus $h\nu$ curves. The E_U of Series A initially decreases to a minimum at x = 0.5 mol% V_2O_5 before generally increasing for x > 0.5 mol% [inset Fig. 7 (a)]. For Series B, the E_U showed decreasing trend until y = 2.0 mol% with Er_2O_3 addition and a small increased for y = 3.0 mol% [inset Fig. 7 (b)].

The refractive index (n) of the two different series of glasses was measured from Abbe refractometer. The variations of n against the V_2O_5 and Er_2O_3 concentration (Fig. 7) displayed opposing behavior to E_{opt} of each series of glasses as shown in Table 3. The n decreases from x = 0

Table 3
Optical energy band gap (E_{opt}), Urbach energy (E_U), refractive index (n) and bonding parameters (β^- and δ) for both series glasses.

Glass ID	E_{opt} (eV)	E_U (eV)	n ±0.001	$\overline{\beta}$	δ
Series A [$20Na_2O$–$20CaO$–$(59-x)B_2O_3$–xV_2O_5–$1Er_2O_3$]					
V0	2.84	0.2052	1.573	1.0019	−0.1939
V0.5	2.97	0.1396	1.556	1.0021	−0.2049
V1.0	2.95	0.1428	1.565	1.0023	−0.2303
V1.5	2.88	0.1722	1.580	1.0019	−0.1939
V2.0	2.66	0.2702	1.591	1.0019	−0.1939
V2.5	2.67	0.2619	1.588	1.00239	−0.2386
Series B [$20Na_2O$–$20CaO$–$(58.5-y)B_2O_3$–$1.5V_2O_5$–yEr_2O_3]					
E0 [7]	1.53	0.6730	1.654	–	–
E1.0	2.88	0.1722	1.580	1.0019	−0.1939
E2.0	2.93	0.1461	1.567	1.0021	−0.2120
E3.0	2.89	0.1578	1.570	1.0020	−0.1949

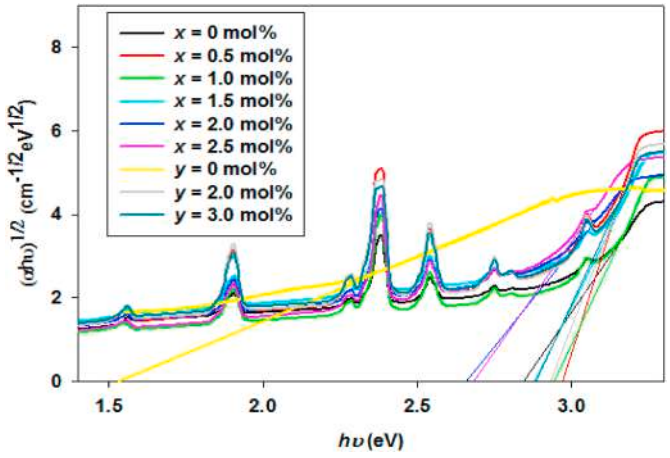

Fig. 6. The Tauc's plots of all glass samples.

mol% to $x = 0.5$ mol% and then followed by an increasing trend beyond $x = 0.5$ mol% of V_2O_5 concentration. However, it is observed that the value of n decreased as the Er_2O_3 content increased at $0 \le y \le 2$ mol% and slightly increased for $y = 3.0$ mol%.

The experimental oscillator strengths (f_{exp}) of the observed $4f$ electronic transitions in the Er^{3+} ions are obtained from the intensity of absorption bands by using relation [17]:

$$f_{exp} = 4.318 \times 10^{-9} \int \alpha(\nu) d\nu \quad (13)$$

where $\alpha = OD/C_m d$ is the molar extinction coefficient at average energy ν (cm^{-1}), OD is the optical density, C_m is the molar concentration of the Er^{3+} ions, and d is the thickness of the glass. The f_{exp} of the glasses have been evaluated from the area under absorption bands in the absorption spectra of the Er^{3+} ion–doped glasses. The strongest absorption band intensity was observed at 521 nm and corresponded with the $^4I_{15/2} \rightarrow {}^2H_{11/2}$ transition; this band obeyed the selection rules $|\Delta L| \le 2$ and $|\Delta J| \le 2$. The transition is known as a hypersensitive transition possessing the largest f_{exp} value [38]. The variation of the f_{exp} for the hypersensitive transition with V_2O_5 content showed an initial strong increase reaching a maximum for $x = 0.5$ mol%, followed by a large drop at $x = 1.0$ mol% Fig. 8 (a), However, addition of $x > 1.5$ mol% V_2O_5 caused a weak increase in f_{exp}. For Series B, the f_{exp} for the hypersensitive transition decreased when Er_2O_3 was added in this glass [Fig. 8 (b)].

In particular, the f–f transitions were predominantly induced by an electric dipole, whereas the contribution of magnetic dipole was negligible. The calculated oscillator strength (f_{cal}) of an electric dipole transition from initial state to an excited state is analyzed from the

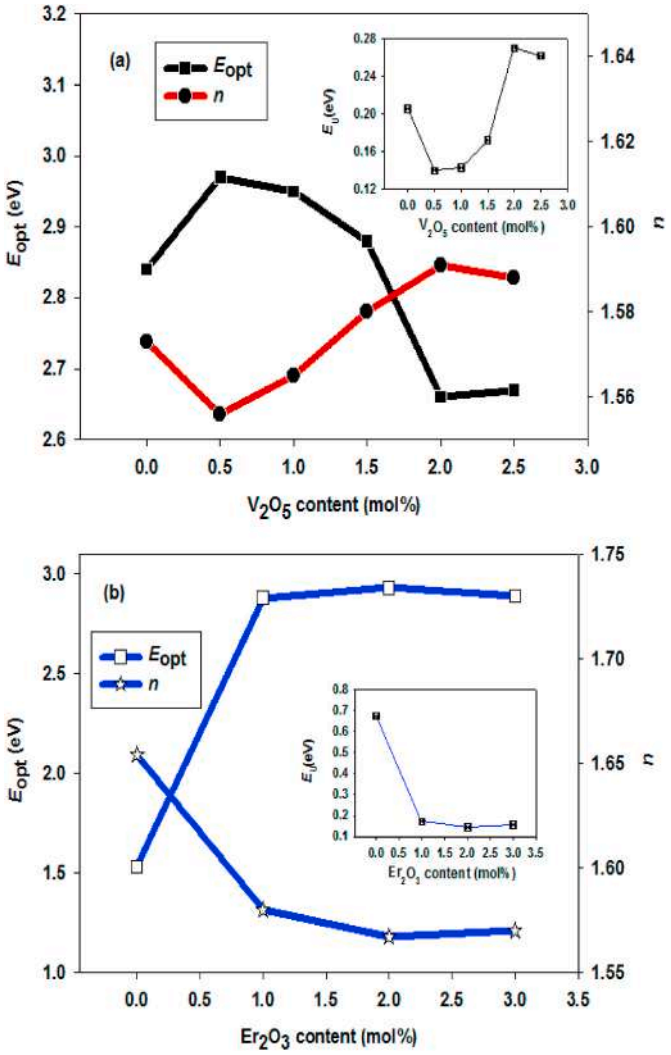

Fig. 7. The variation of optical band gap (*E*opt) and refractive index (n) of (a) 20Na2O–20CaO–(59 – x)B2O3–xV2O5–1Er2O3 (x = 0–2.5 mol%) and (b) 20Na2O–20CaO–(58.5 – y)B2O3–1.5V2O5–yEr2O3 (y = 0–3.0 mol%) glass samples. Insets show the variation of Urbach energy (*E*u) with V2O5 and Er2O3 contents.

Judd–Ofelt (J–O) theory using the equation [39].

$$f_{cal} = \frac{8\pi^2 mc\nu}{3h(2J+1)} \left[\frac{(n^2+2)^2}{9n}\right] \times \sum_{\lambda=2,4,6} \Omega_\lambda \left(\psi J U^\lambda \psi' J'\right)^2 \quad (14)$$

where m refers to the mass of the electron, c is the velocity of light in vacuum, h is the Planck's constant, n is the refractive index of the glass, J is the total angular momentum of the ground state, ν is the frequency of the transition $\Psi J \rightarrow \Psi' J'$, Ω_λ are the J–O intensity parameters and $||U^\lambda||^2$ are the doubly reduced matrix elements of the unit tensor operator [40].

3.3.2. Judd–Ofelt parameters and bonding properties

J–O intensity parameters (Ω_λ) are used to describe the bonding, symmetry and rigidity of the host matrices [41]. These values were calculated from the experimentally measured values of oscillator strength f_{exp} for the different transitions under the least squares fitting method. The compositional dependence of the J–O parameters are presented in the inset of Fig. 8 (a) and **8 (b)**, which show the variation of J–O parameters with the substitution of V_2O_5 and E_2O_3 in Series A and B glasses, respectively. As shown in both figures, the trends of the J–O parameters almost similar to the f_{exp} behavior except for Ω_6 of Series B.

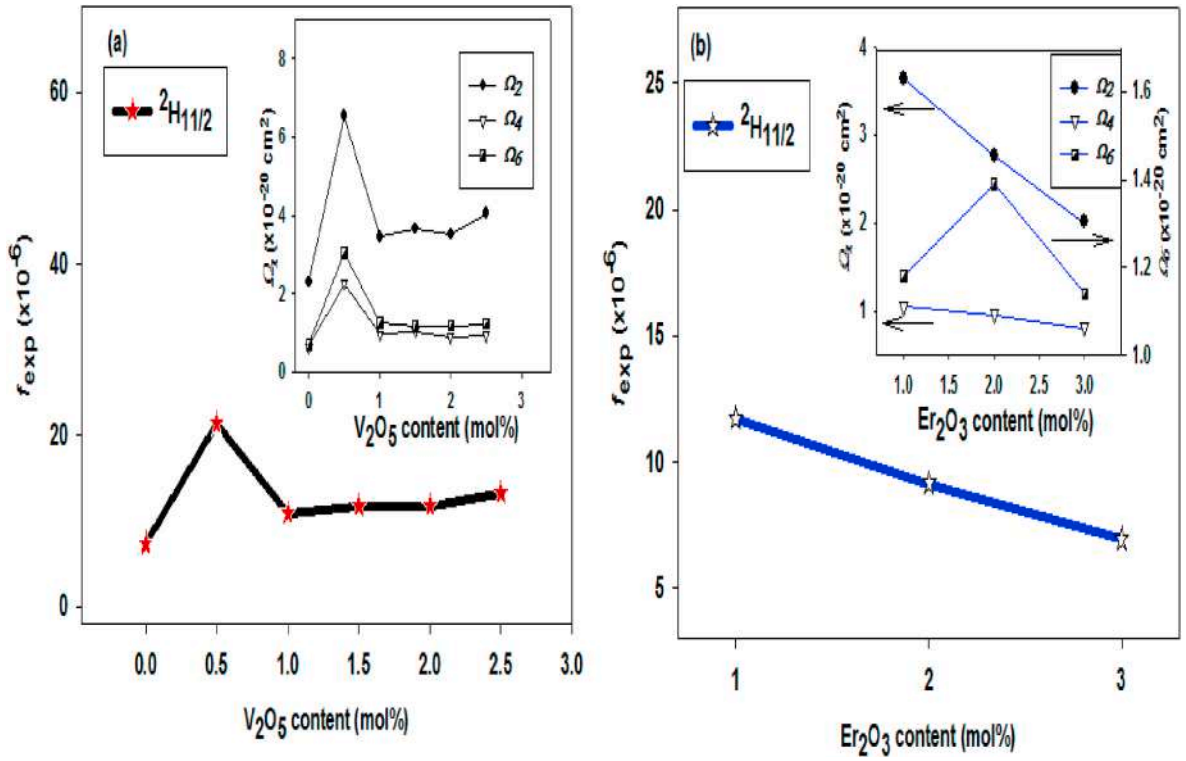

Fig. 8. (a) The variation of oscillator strength (f_{exp}) of transition $^4I_{15/2} \rightarrow {}^2H_{11/2}$ of Er^{3+} with V_2O_5 content in $20Na_2O$–$20CaO$–$(59 - x)B_2O_3$–xV_2O_5–$1Er_2O_3$ glasses. (b) The variation of oscillator strength (f_{exp}) of transition $^4I_{15/2} \rightarrow {}^2H_{11/2}$ of Er^{3+} with Er_2O_3 content in $20Na_2O$–$20CaO$–$(58.5 - y)B_2O_3$–$1.5V_2O_5$–yEr_2O_3 glasses. Insets show the variation of the Judd–Ofelt parameter (Ω_λ) of Er^{3+} in the both glass systems.

All J–O parameters (Ω_2, Ω_4 and Ω_6) in glass Series A are increased up to $x = 0.5$ mol% and then decreased at $x = 1.0$ mol% V_2O_5 [(inset Fig. 8 (a)]. Contrary, Ω_2 and Ω_4 for Series B are observed to decrease with increasing Er_2O_3 contents, while Ω_6 showed maximum value at $y = 2.0$ mol% [inset Fig. 8 (b)].

The bonding properties of the glasses which were calculated using following equations [16] are also presented in Table 3:

$$\delta = \left(\frac{1-\overline{\beta}}{\overline{\beta}}\right) \times 100 \tag{15}$$

where $\overline{\beta} = \sum \frac{\beta}{N}$ and β(nephelauxetic ratio) $= \frac{\nu_c}{\nu_a}$. ν_c and ν_a are the observed wave numbers (in cm^{-1}) of a particular transition of the Er^{3+} in the glass host and in the aqueous solution, respectively. The positive or negative sign value of δ indicates the covalent or ionic nature of bonding between the Er^{3+} and ligand field. In Series A glasses, the magnitude of δ varies nonlinearly and shifts to average a higher negative value with V_2O_5 addition in borate network, whereas for Series B, δ shows an increase in negative value up to $y = 2.0$ mol% Er_2O_3 but decreased at $y = 3.0$ mol% Er_2O_3. The small variation in δ shows that the electronic transition energy level experienced only slight changes in position with changes in V_2O_5 and Er_2O_3 content [13,31].

3.4. Elastic properties

The computed values of longitudinal modulus (C_L), shear modulus (μ), Young's modulus (Y) and Debye temperature (θ_D) for both series of glasses are given in Table 4. The variation of elastic moduli with V_2O_5 addition is presented in Fig. 9 (a). In Series A glass, the C_L, μ and Y clearly rose at $x = 0.5$ mol% V_2O_5, followed by a decrease with further addition of V_2O_5, except for C_L, which became nearly constant at $x \geq 1.5$ mol%. Moreover, as observed in the inset of Fig. 9 (a), the θ_D showed a similar behavior to those of elastic moduli; this temperature increased at $x = 0.5$ mol% and decreased for $x \geq 1.0$ mol%. Meanwhile for Series B,

Table 4
Values of longitudinal modulus (C_L), shear modulus (μ), Young's modulus (Y) and Debye temperature (θ_D) for both series of glasses.

Glass ID	C_L	μ	Y	θ_D
	GPa	GPa	GPa	K
	±0.4	±0.1	±1	±1
Series A [$20Na_2O$–$20CaO$–$(59 - x)B_2O_3$–xV_2O_5–$1Er_2O_3$]				
V0	70.9	25.5	62	496
V0.5	93.1	39.0	89	607
V1.0	77.1	23.1	59	473
V1.5	78.1	22.2	58	464
V2.0	76.3	18.4	49	424
V2.5	77.3	16.3	45	400
Series B [$20Na_2O$–$20CaO$–$(58.5 - y)B_2O_3$–$1.5V_2O_5$–yEr_2O_3]				
E0 [7]	89.5	29.3	74	538
E1.0	78.1	22.2	58	464
E2.0	75.4	20.7	54	440
E3.0	72.7	19.9	52	424

Fig. 9 (b) shows a large decrease in C_L, μ, Y and θ_D, respectively with initial addition of Er_2O_3 at $y = 1.0$ mol% before small decrease between $y = 2.0$ mol% and $y = 3.0$ mol%. The decrease in elastic moduli and θ_D indicate decrease in rigidity and all modes of vibration in glasses decreased with Er_2O_3.

3.5. Photoluminescence spectra

Fig. 10 (a) and 10 (b) illustrate the up–conversion PL spectra of the studied glasses excited with 779 nm light. The observed emission bands for these glass systems appeared at a shorter wavelength than the excitation wavelength. Three emission bands at 518 nm (green), 556 nm (green) and 647 nm (red) were observed due to the Er^{3+}: $^2H_{11/2} \rightarrow {}^4I_{15/2}$, $^4S_{3/2} \rightarrow {}^4I_{15/2}$ and $^4F_{9/2} \rightarrow {}^4I_{15/2}$, transitions, respectively [10,13]. An additional band was also detected at 590 nm in the PL spectra [42–44]

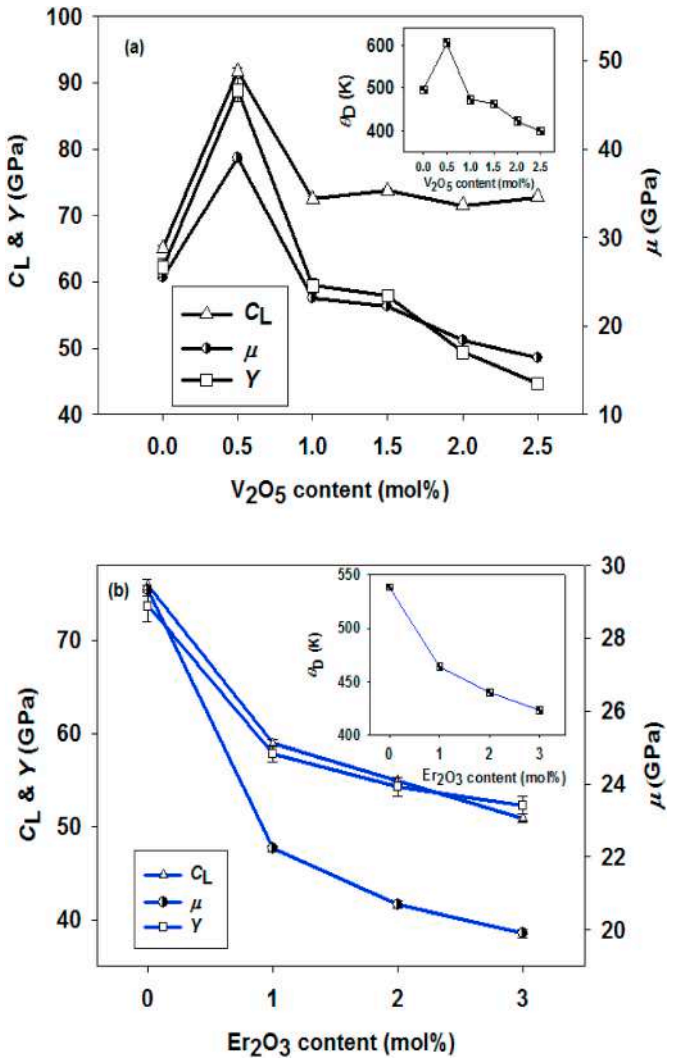

Fig. 9. Plot of longitudinal modulus (C_L), shear modulus (μ) and Young's modulus (Y) of (a) $20Na_2O$–$20CaO$–$(59-x)B_2O_3$–xV_2O_5–$1Er_2O_3$ ($x = 0$–2.5 mol %) and (b) $20Na_2O$– $20CaO$–$(58.5-y)B_2O_3$–$1.5V_2O_5$–yEr_2O_3 ($y = 0$–3.0 mol%) glass samples. Insets show the Debye temperature (θ_D) of the glass samples.

related to transition $^2B_1 \rightarrow {}^2B_2$ of V^{4+} ions. The highest intense peak was detected at 647 nm while a lower peak was at 556 nm and intensities of all the bands were found to be concentration dependent. Fig. 10 (c) presents all emission bands versus V_2O_5 content. It is very clear that the PL intensity increases with the concentration from 0 to 0.5 mol% and further addition of V_2O_5 for 0.5 mol% $< x <$ 1.5 mol% caused a reduction in the band intensities. Beyond 1.5 mol%, the intensities are observed to increase back. Meanwhile, the emission band intensities of Series B [Fig. 10 (d)] significantly enhanced with Er_2O_3 content from 1.0 mol% to 2.0 mol% before a decrease occurred at $y = 3.0$ mol%. Although the addition of Er_2O_3 to the lowest PL sample $x = 0.5\%$ V_2O_5 in Series A has caused the PL to increase in Series B, the increment is lower than the maximum PL achieved by sample $x = 0.5$ mol % V_2O_5. The possible mechanisms for the up–converted emission has been illustrated in Fig. 11.

3.6. Decay lifetime

The decay profiles of the luminescence from $^2B_1$ level of $20Na_2O$–$20CaO$–$58.5B_2O_3$–xV_2O_5–$1Er_2O_3$ ($x = 1.0$ and 2.0 mol%) and $20Na_2O$–$20CaO$–$(58.5-y)B_2O_3$–$1.5V_2O_5$–yEr_2O_3 ($y = 1.0$ and 2.0 mol %) glass samples has been measured by monitoring V^{4+} emission at 580 nm under excitation at 779 nm, as shown in Fig. 12. The curve is analyzed by using second order exponential decay as follows [45]:

$$I(t) = I_0 + A_1 exp\left(\frac{-t}{\tau_1}\right) + A_2 exp\left(\frac{-t}{\tau_2}\right) \quad (16)$$

where $I(t)$ stand for the intensity of luminescence at time t, I_o is the background light intensity, τ_1 and τ_2 are the short and long lifetimes with corresponding intensity coefficients, A_1 and A_2, respectively. The first term of equation is related to the excited state absorption with short lifetime of τ_1 while the later one is related to the process of energy transfer with long lifetime of τ_2. Then, the experimental lifetime (τ_{exp}) is calculated using the relation:

$$\tau_{exp} = \frac{A_1\tau_1^2 + A_2\tau_2^2}{A_1\tau_1 + A_2\tau_2} \quad (17)$$

The τ_{exp} of the excited $^2B_1$ level have been obtained by taking first e-folding times of the decay curves. The decay lifetime (τ_{exp}) of V^{4+} were determined to be 27.5 and 3.1 corresponding to $x = 1.0$ and 2.0 mol% V_2O_5, respectively. Meanwhile the τ_{exp} value is decreasing from 52.4 to 42.9 ns when the Er_2O_3 concentration is increasing from $y = 1.0$–2.0 mol %.

4. Discussions

Our FTIR result showing the presence of VO_4, VO_5, BO_3 and BO_4 structural units confirmed the formation of both BO and NBO in the glass network. In Series A glass, the increase in the relative area of BO_3 functional groups with addition of V_2O_5 throughout the glass system corresponded to the increase in the number of NBO [Fig. 3 (a)]. On the other hand, number of BO increased for $x \leq 1.0$ mol% and starts to decrease beyond $x = 1.0$ mol% as indicated by the changes in relative area of the BO_4/V═O assigned peaks. Moreover, the shift in the assigned BO_4/V═O band $x > 1.0$ mol% could be due to vibrational frequencies of the V═O vanadyl group in the VO_5 tbp unit. The band in this region shifted toward lower frequencies (901 cm^{-1}) indicates the decrease in number of BO. For Series B [Fig. 3 (b)], at $y < 2.0$ mol%, the increase in the relative area of BO_3 shows that the number of NBO increased and for $y = 3.0$ mol%, the BO_3 relative area decreased, indicating the decrease in the formation of NBO.

Density measurement is considered as an important physical tool for exploring any structural change with the variation in glass composition in a glass network [43]. The change in density (ρ) in studied glass system is due to alteration in on the molar mass (M) and molar volume (V_a) of the glasses. The increase in ρ with V_2O_5 addition at a fixed Er_2O_3 content [Fig. 2 (a)] in Series A glass can be caused by replacing lighter oxide B_2O_3 (0.0696 kg mol^{-1}) with heavier metal oxide V_2O_5 (0.1819 kg mol^{-1}), which leads to an enlarged increment in the average molar weight of the glass system. In general, the molar volume (V_a) of the glass system is expected to increase as V_2O_5 with larger molecular volume (54.13 cm^3 mol^{-1}) replaces B_2O_3 (12.57 cm^3 mol^{-1}). However, the nonlinear increase in V_a [Fig. 2 (a)] with lower rate of increase below $x = 0.5$ mol% to $x = 1.0$ mol% followed by a larger increase for $x > 1.0$ mol% can be explained by the altered role of V_2O_5 from the former ($x \leq 1.0$ mol%) to a modifier ($x > 1.0$ mol%), as indicated by FTIR results [Fig. 3 (a)]. For $x \leq 1.0$ mol%, although FTIR showed competition between the formation of BO and NBO, the relative area of BO_3 which indicate the increase in NBO concentrations are more dominant compared to the increase in BO represented by the BO_4/V═O relative area. However, the formation of BO in the region would weaken the expansion of the glass network that led to a slightly slower increase in V_a, thereby increasing the increment rate of ρ. Meanwhile, the rapid decrease in relative areas of the BO_4/V═O at $x > 1.0$ mol% indicate a large decrease in BO in the glass system [Fig. 3 (a)]. Similarly, the relative areas of BO_3 rose correspondingly with the increase in NBO. Therefore, the observed large increase in V_a at $x > 1.0$ mol% may be due

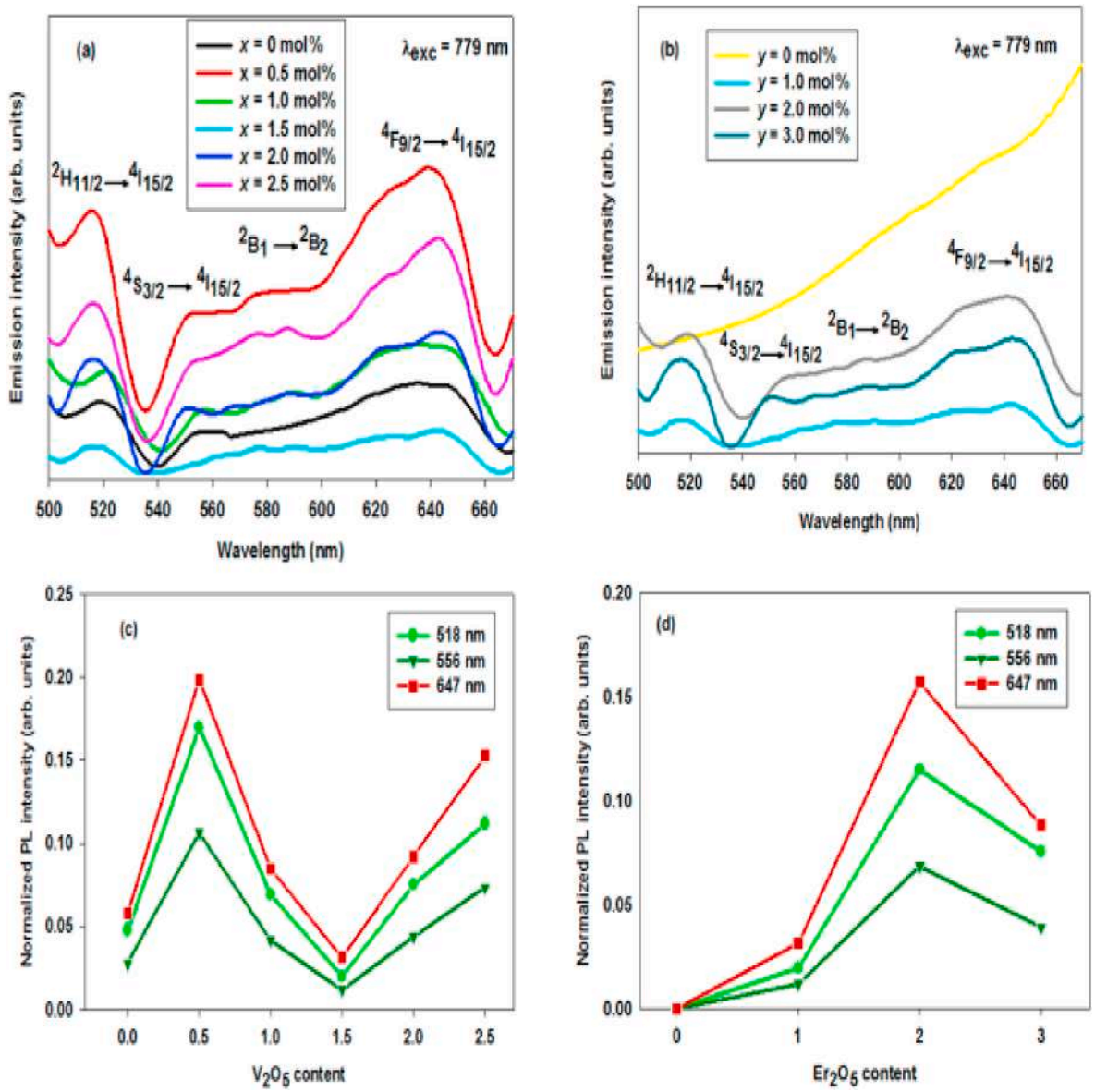

Fig. 10. (a) Up–conversion spectra of $20Na_2O–20CaO–(59 – x)B_2O_3–xV_2O_5–1Er_2O_3$ (x = 0–2.5 mol%) glass samples. (b) Up–conversion spectra of $20Na_2O–20CaO–(58.5 – y)B_2O_3–1.5V_2O_5–yEr_2O_3$ (y = 0–3.0 mol%) glass samples. (c) The normalized photoluminescence intensity as a function of V_2O_5 content. (d) The normalized photoluminescence intensity as a function of Er_2O_3 content.

to the influence of the modifying role of V_2O_5 that led to BO breakage to form NBO in the glass structure. The increase of NBO reduced the network connectivity of the glass, causing the glass on the whole became further open, which resulted in decelerated increase in ρ.

For Series B, the increase in ρ for $0 \leq y \leq 3.0$ mol% [Fig. 2 (b)] is attributed to the substitution of a heavier metal oxide Er_2O_3 at the expense of the lighter oxide B_2O_3 with a lower molar mass than that of Er_2O_3 (0.3826 kg mol^{-1}). As found for Series A, the glass with composition y = 1.0 mol% was already in the region where NBO was more dominant, and the concentration of NBO was expected to persistently rise with further substitution of Er_2O_3. As expected, NBO formed with Er_2O_3 addition and thus increased the V_a [Fig. 2 (b)]. The increase in V_a can be explained as a result of the breakage of the B–O–B linkages, which thereby increase the opening up of the glass network. Earlier studies of some other glasses have reported the high potential of Er_2O_3 to participate as modifier in the glass network [44]. In the present glass, the suggested dope of Er_2O_3 as network modifier can be further corroborated with the FTIR result [Fig. 3 (b)] which showed an increase in the relative area of assigned BO_3 bond vibrations. This result implies an increase in NBO content, which explains the rapid rate of increase in V_a at $y \leq 2.0$ mol%. Meanwhile, the ρ increased strongly for y = 3.0 mol% [Fig. 2 (b)] as the molar mass of the glass was increased uniformly as well as was accompanied by gradually increasing V_a. The observed decelerated increase in V_a for y = 3.0 mol% [Fig. 2 (b)] can be understood by considering the retardation of formation of NBO and the Er^{3+} ion was suggested to be located interstitially in the glass network [46]. In Table 2, the smaller percentage increase in ρ for Series A glasses than for Series B glass system can be suggested because of the relatively small amount of V_2O_5 added to this glass while the concentration of Er_2O_3 with the heaviest molar mass was fixed and that of borate was reduced. Therefore, we assumed that the density of the glasses was greatly affected in the succession of $B_2O_3 < V_2O_5 < Er_2O_3$.

The absorption spectra of rare earth ions provide useful information about the radiative property of significant energy level [47,48]. Figs. 4 and 5 showed the appearance of ten absorption bands in both series of glasses corresponded to the 4f–transition of Er^{3+} ions from $^4I_{15/2}$ ground state to various excited states. The assignment bands in these glasses agree with previous reports which indicate the successful introduction of

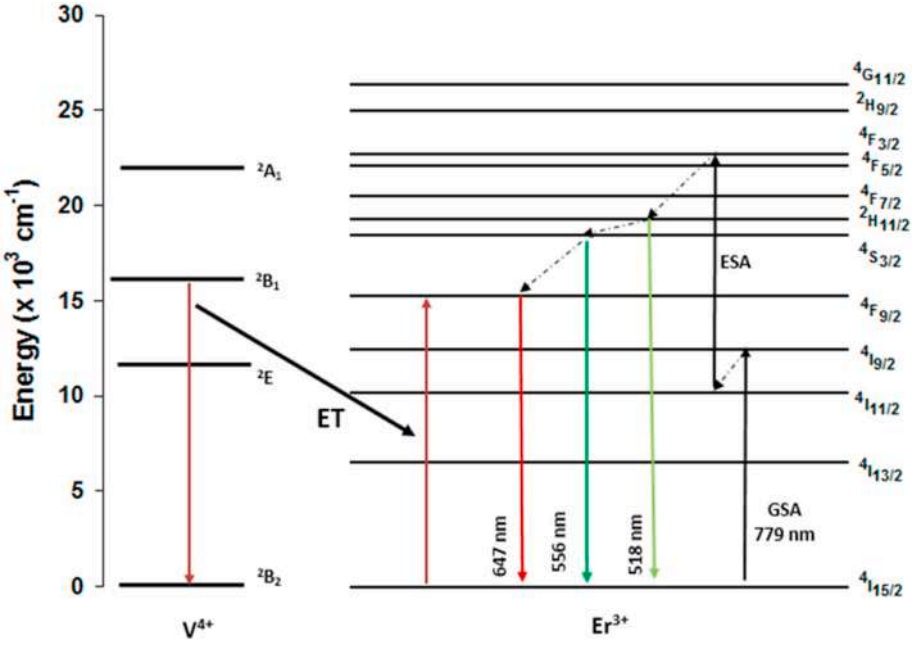

Fig. 11. Partial energy level diagram of the V^{4+} and Er^{3+} ions illustrating possible up–conversion pathway and energy transfer process.

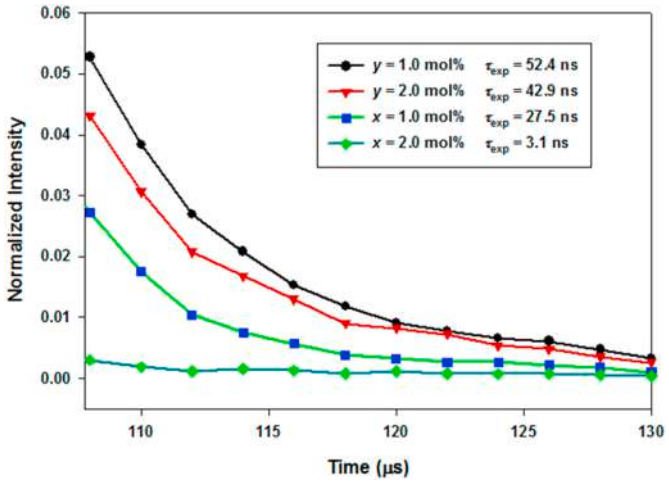

Fig. 12. Decay curves of V^{4+} in borate glasses under excitation at 779 nm.

Er^{3+} ions as dopant in the glass matrix [31]. Meanwhile, vanadium ions in general are known to exhibit several absorption bands because of possible valences of V^{4+} [49,50]. For vanadyl ions, three absorption bands can exist on the basis of energy level scheme of VO^{2+} ions in a ligand field C_{4v} symmetry corresponding to the transitions $^2B_2 \rightarrow {}^2A_1$ (330–475 nm), $^2B_2 \rightarrow {}^2B_1$ (580–715 nm) and $^2B_2 \rightarrow {}^2E_g$ (875–1000 nm) [43]. In the present glasses, only the second transition is detected. The small kink at about 590 nm in the Er_2O_3–free sample ($y = 0$ mol%) (inset Fig. 5) of the glass sample was assigned to the $^2B_2 \rightarrow {}^2B_1$ transition of V^{4+} ions with d^1 configuration [34,43]. Our results therefore suggest that the bands observed in the optical absorption spectra of V_2O_5/Er_2O_3 co–doped borate glasses in the present study represents the characteristic absorption of distorted octahedral site symmetry related to the *d–d* transition of V^{4+} ions and the *f–f* transition of Er^{3+} ions.

In amorphous materials, the study of optical absorption edge near UV region is useful to determine optical band gap energy of glasses which involve electron excitation in valence band to unoccupied state in the conduction band [51]. The optical band gap can reveal additional structural information and the nature of chemical bonds in these glasses.

In the presently studied glass, the variation in E_{opt} was discussed in terms of variation of BO and NBO concentrations. The maximum E_{opt} at $x = 0.5$ mol% [Fig. 7 (a)] in Series A reflects the formation of BO created by V_2O_5 in the host matrix. Meanwhile, the decrease in E_{opt} for $x > 0.5$ mol % in the glasses was suggested to be due to the increase in NBO by the formation of BO_3 in the glass system as indicated by FTIR. Previous studies reported that NBO formation weakens the glass structure and causes the electrons to be less tightly bound [52,53]. Hence, more electrons can be excited from the valence band to the conduction band. Thus, this finding reflects a reduction of E_{opt} for $x \geq 1.0$ mol% and implies an increasing degree of disorder caused by V_2O_5 as a modifier. In addition, the variation of E_{opt} is accompanied by defect concentration in the energy band, which is represented by E_U. The relationship between E_{opt} and E_U [inset Fig. 7 (a)] indicates that the addition of V_2O_5 at $x = 0.5$ mol% decreased E_U, suggesting that decreases in defects formed below the conduction band is also the reason behind the increased E_{opt} ($x = 0.5$ mol%). The addition of V_2O_5 for $x > 0.5$ mol% creates more defects as indicated by larger E_U, thereby decreasing the E_{opt} of the glasses. The minimum refractive index (n) at $x = 0.5$ mol% [Fig. 7 (a)] also corresponded to the maximum E_{opt}. The decrease in n can be understood in relation to the increase in BO concentration at $x \leq 0.5$ mol%, whereas the increase in n relates to the increase in NBO at $x > 1.0$ mol% which possesses large polarizability. The formation of covalent bond through formation of VO_5 together with BO_4 units is expected to build more rigid glass structure. The formation of BO holds an electron cloud tightly, which reduces electronic polarizability and thus decreases n for $x \leq 0.5$ mol%. By contrast, the increase in BO_3 units having NBO exerts the opposite effect; V_2O_5 as a modifier tends to break the glass network and create NBO, which gives rise to higher electronic polarizability and causes n to increase for $x > 1.0$ mol% [51,54].

For Series B, the behavior of E_{opt}, E_u and n [Fig. 7 (b)] as a result of increasing Er_2O_3 showed that the small doping of Er_2O_3 has a significant effect on the optical properties of the glasses. The observed decreased in E_u can be attributed to the replacement of Er_2O_3 at B_2O_3 sites in the glass network, which disturb the number of defect states and consequently reduce the localized states within the band gap, causing increment of the E_{opt} value [55]. The variation in E_{opt} with Er_2O_3 content did not, however, correspond to the increase in NBO as evident by the FTIR results. The E_{opt} trend of the present study are similar to other reported rare–earth doped oxide glasses [1,55,56].

The magnitude of experimental oscillator strength (f_{exp}), which is calculated from the relative area of individual electronic transition, describes the probability of absorption of electromagnetic radiation between energy levels of *f–f* transition in rare earth ions [57]. In contrast to transition metal ions with partially filled 3*d* orbitals, RE ions contain unpaired electrons in the 4*f* orbitals. Generally, the 4*f* electrons in RE ions are not significantly affected by changes in the ligands because the electrons are well shielded by 5*s* and 5*p* electrons from outside. However, hypersensitive transition was considered as an exceptional *f–f* transition, with an intensity peculiarly sensitive to small changes in the surrounding environment. The *f– f* transitions are forbidden by an electric dipole mechanism because the parity does not obey the Laporte selection rule where the parity between states should be inverted. The dynamic coupling model which describes the interaction between 4*f* electrons with transient electric dipoles induced in the surrounding ligands by the incident radiation field has been proposed to explain the enlarged f_{exp} variation for hypersensitive transition. In the present glass system, the hypersensitive transition ($^4I_{15/2}$ to $^2H_{11/2}$) exhibits an increased f_{exp} compared with the other transitions and thus shows its dominant effect on the surrounding environment of Er^{3+} ions and polarizability of ligands [31]. The f_{exp} of hypersensitive transition in both Series A and Series B are strongly dependent on dopant concentration. The f_{exp} provides indirect information on the symmetry and bonding of RE ion within the matrix [40].

For glass in Series A, the large increase in f_{exp} of the hypersensitive transition **[**Fig. 8 (a)**]** from 7.35×10^{-6} ($x = 0$ mol%) to 21.4×10^{-6} ($x = 0.5$ mol%) indicates that the glass samples exhibit an increased asymmetry of electric field acting around the Er^{3+} ions sites. The f_{exp} maximum at $x = 0.5$ mol% was attributed to an increase in asymmetry around Er^{3+} ions because of the irregularity in bond length as the VO_5 functional group was introduced into the glass network besides borate structural units. This result agrees with our FTIR vibrational analysis, which shows an increase in relative area of VO_5 units with addition of V_2O_5 ($x = 0.5$ mol%) [Fig. 3 (a)**]**. This result indicates that V_2O_5 serves as a network former. When V_2O_5 was introduced, the Er^{3+} ions experience uneven electric field inside the host glass because of the substitution of an enlarged bond length of V–O relative to B–O bonds besides the changes in bond angles [16]. However, for $x = 1.0$ mol%, the drop in f_{exp} for hypersensitive transition indicates a decrease in asymmetry of ligand field around Er^{3+} ions. This effect is possible as higher V_2O_5 content reduces the inhomogeneity surrounding Er^{3+} ions and thus reduces asymmetry. Such explanation agrees with a previous literature report [58]. The slight increase in f_{exp} observed for $x > 1.5$ can be understood by considering the role of V_2O_5 as modifier, which forms NBO that reduce symmetry [59] and promote the spread of Er^{3+} ions from sharing the limited NBO in the host glasses. This effect can lower the possibility of Er^{3+} ions clustering and decreasing the interaction amongst Er^{3+} ions which results in high non–radiative losses [60]. Furthermore, previous studies showed that Er^{3+} ion clustering usually occurs at a relatively high Er_2O_3 concentration [61,62]. In this study, we chose to add small amount of Er_2O_3 at 1 mol% throughout all samples in Series A to minimize the clustering of Er^{3+} ions in glasses. The increase in concentration of V^{4+} ions occupies a network–modifying position outside the glass network, and the production of more NBO is indicated by increasing the relative area of BO_3 in the FTIR results. Although NBO is known to contribute to an increase in asymmetry, the recovery in f_{exp} for the hypersensitive transition at 1.5 mol% $\leq x \leq$ 2.5 mol% is weak and was unable to offset the increase in symmetry caused by V_2O_5. In this study, our results also show that the non–hypersensitive transitions produced f_{exp} maximum at $x = 0.5$ mol% with a lower oscillator strength than that of the hypersensitive transition for the same sample. Since dynamic coupling is not involved in non–hypersensitive transitions, the increase in f_{exp} for the transitions indicates the strength of the asymmetry introduced by V_2O_5. Previous reports on $(60 - x)Sb_2O_3$–$35P_2O_5$–$5MgO$–xEr_2O_3 glasses have shown an increase of both oscillator strengths of hypersensitive and non–hypersensitive transitions with increasing Er_2O_3 contents [63].

In order to investigate the effect of the host glass on the optical properties of the Er^{3+} ions, it is interesting to study the relations between J–O parameters and the properties of the glass host. Our observation on J–O parameters (Ω_2, Ω_4 and Ω_6) of this glass system indicates that the variation of J–O parameters depend on the V_2O_5 content, which is ultimately responsible for modifying the local environment of Er^{3+} ions in the glass matrix. The magnitude of J–O parameters for all concentrations in both series of glasses followed $\Omega_2 > \Omega_6 > \Omega_4$. This result indicates that the impact of Ω_2 is greater than those of the other two on the host matrix. According to the J–O theory, Ω_2 depends on crystal field parameters and covalency between rare earth and surrounding ligands [17]. However, crystal field contribution dominates over covalency which pointed out that Ω_2 is more sensitive to crystal field site symmetry and local environment around rare earth ions. Usually, a decrease in symmetry is assigned to an increase in Ω_2 [40]. Therefore, raising the concentration of V_2O_5 at $x = 0.5$ mol% for glass in Series A **[**inset Fig. 8 (a)] led to an increase in asymmetry. Because the calculated value of Ω_2 depends on $|\langle \Psi J \,||U^{(2)}||\Psi' J' \rangle|^2$, where $U^{(2)}$ is largely determined by the hypersensitive transition [31], the Ω_2 values can be directly compared with f_{exp} for the transition. By comparison, the trend of Ω_2 for Series A followed the trend of f_{exp} for the hypersensitive transition in Fig. 8 (a), indicating that the hypersensitive nature of Er^{3+} ion transition of the glass system is strongly dependent on asymmetry. Hence, the observed Ω_2 maximum at $x = 0.5$ mol% supports our earlier suggestion that the f_{exp} maximum for the same glass sample is attributed to the high asymmetry of the sample owing to the presence of V_2O_5 as a glass–forming oxide.

Meanwhile, parameter Ω_4 was reported to increase with decreasing covalence character of RE–O bonding [64]. However, the result run contrary to that reported in other glasses [65,66]. As such, the relationship between Ω_4 and RE–O covalency is still not conclusive. It has been reported that $\Omega 4$ was influenced by the glasses' bulk properties, such as the rigidity and viscosity of the host matrix, which affect the bonds between rare earth ion and ligand atoms [58], while ligand symmetry is not directly related to Ω_4 [54]. In the present glasses, the variation of Ω_4 with V_2O_5 which showed maximum at $x = 0.5$ mol% **[**inset Fig. 8 (a)] in Series A is associated with the increase rigidity of glass contributed by an increase in bridging oxygens, as indicated by FTIR. In this case, V_2O_5 strengthened the glass structure and increased the degree of cross–linking through the formation of new V–O bonds with gradual reduction in the rate of formation of NBO in the glass network [66]. Interestingly, the composition ($x = 0.5$ mol%), where Ω_4 was maximum, coincided with the composition that showed the highest value of Ω_2 at $x = 0.5$ mol%. This finding demonstrated that the increase in rigidity is related to the asymmetry of the glasses. Nevertheless, the decrease in $\Omega 4$ for $x \geq 1.0$ mol% indicates the weakening of network rigidity caused by the formation of NBO considering the modifier action of V_2O_5 on the glasses. Thus, this result suggests a gradual increase in the structural depolymerization of the glasses for $x > 1.0$ mol%; this finding is also consistent with the observed larger increase in V_a **[**Fig. 2 (a)**]** and BO_3 units [Fig. 3 (a)]. That indicates reduced cross–linking in these glasses. Furthermore, the effect of V_2O_5 addition on bulk rigidity is evidenced by our ultrasonic results [Fig. 9 (a)], where the substitution of V_2O_5 at $x = 0.5$ mol% strengthened the glass network as additional BO_4/V═O units were formed, which increased the rigidity/stiffness of the glass network as reflected by the initial increase in C_L, μ and Y. However, NBO formation increased with further addition of V_2O_5 at $x \geq 1.0$ mol% and led to an open structure and reduced rigidity/stiffness. Ultimately, the elastic modulus decreased. Y and μ decreased for $x > 1.0$ mol% V_2O_5, whereas C_L remained constant on the average with an increase of V_2O_5 content. Thus, the drop in Y for $x > 1.5$ mol% appeared to be dominated by the behavior of μ. Interestingly, the variation of Debye temperature (θ_D) **[**inset Fig. 9 (a)] was also in accordance with the variation of Ω_4 J–O parameter; this notation supports our earlier discussion on the elastic rigidity of glasses. Therefore, the maximum value

of θ_D at $x = 0.5$ mol% suggests that the rigidity was the highest for the glass sample compared with the other glasses in the series. By contrast, the drop in θ_D confirms that overall rigidity decreases for $x \geq 1.0$ mol%.

For many instances, Ω_6 was also found to be affected by rigidity of host medium [58] but other study reported that value of Ω_6 is inversely proportional to the covalence character of RE–O bonding [60]. The similar trend between Ω_6 [inset Fig. 8 (a)] variation and ultrasonic results [Fig. 9 (a)] confirm that rigidity of glass host strongly affected on Ω_6 parameter. Also, the highest value of Ω_6 for sample $x = 0.5$ mol% in Series A glasses is indication for the lower covalent nature of Er^{3+} with the ligands, which was responsible for the high ionicity environment of this glass sample. In addition, the investigation on bonding parameter δ showed a shift in δ with respect to that of the aqueous solution for all the glass samples in Series A (Table 3). This occurrence resulted in the negative sign value of δ that indicates a decreased covalency in the environment of the Er^{3+} and surrounding ligands upon V_2O_5 addition in a borate network.

On the other hand, the glasses in Series B also showed that the f_{exp} of the hypersensitive transition appeared with a similar trend to the Ω_2 [Fig. 8 (b)] with increasing Er_2O_3 content. In general, the Er_2O_3 act as modifier and oxygen of the modifier breaks the local symmetry of glass network and creating NBO. It is expected that an average distance between network bonds become larger causing the average distance of Er–O ionic bond to increase. The Er^{3+} ions surrounding these distant ligands experience weaker crystal field which leads to a decrease in the Ω_2 value. Yet, another reason for the decrease in Ω_2 is suggested due to dwindling of covalency of Er–O bond, as supported from calculation of bonding parameter, δ. Our results showed that the increase in δ to a more negative value with Er_2O_3 addition of up to 2 mol% (Table 3) indicates the less covalent nature of chemical bond with the ligands which was responsible for the increase in ionicity. Therefore, the decrease in Ω_2 at $y = 2.0$ mol% [inset Fig. 8 (b)] was in tandem with the decrease in δ as expected due to increase in ionicity. The increase in ionicity of Er–O bond is also expected as molar volume of the glasses increased as shown in Fig. 2 (b). These results support the viewpoint that there is increase in formation of NBO contributed by modifying action of Er_2O_3 in the glasses which corresponded to the increase of ionic bonds. However, the increased Er_2O_3 content within borate glass with decreased NBO formation at $y = 3.0$ mol%, revealed by FTIR caused the Er^{3+} ions to cluster around a smaller number of anionic sites [13]. The clustering of Er^{3+} ions may not occur at $y = 2.0$ mol% because of the presence of an increased number of NBO, whereas the Er^{3+} ion concentration was exceedingly low to cause clustering at $y = 1.0$ mol%.

In Series B glass matrix, the decrease in J–O parameter Ω_4 [inset Fig. 8 (b)] indicates reduction in network rigidity with increasing Er_2O_3 content. Based on elastic results, the observed decrease in C_L, μ, Y and θ_D [Fig. 9 (b)] were mainly due to the increase of the number of NBO as a direct effect of addition of Er_2O_3 modifier content to the glass network structure which consequently reduces the glass rigidity. Further support that the addition of Er_2O_3 leads to depolymerization of glass network and promotes the formation of a high number of NBO can also be viewed from the increase in V_a for $y = 0$–2.0 mol% [Fig. 2 (b)]. However, the increase in clustering caused by the large addition of Er_2O_3 at $y = 3.0$ mol% did not significantly assist the rigidity of the glasses.

Meanwhile, Ω_6 was maximum at $y = 2.0$ mol% [inset Fig. 8 (b)] indicating the NBO increased with the increase of Er_2O_3 concentration resulting in lower covalency of Er–O bond. As mentioned earlier, bulk rigidity of glass could be one of the factors that influences parameter Ω_6. However, Ω_6 for Series B was found to be less affected by the bulk rigidity of the glass, as both elastic moduli and θ_D [Fig. 9 (b)] showed different behavior with Ω_6.

Based on absorption spectra, the longer absorption wavelength in the visible spectrum was chosen for attaining up–conversion PL spectra of Er^{3+} ions. As a result, both series of glasses achieved higher energy emissions in the visible spectrum under lower–energy excitations [(Fig. 10 (a) and 10 (b)]. In the figures, the up–converted emission bands of green (518 nm and 556 nm) and red (647 nm) emissions were assigned to the transitions of Er^{3+}. Usually, Er^{3+}–doped glasses show two strong visible emissions at green region upon excited under ~800 nm light [10,40,68]. These green emissions are attributed to excited–-state absorption (ESA) process, whereas an additional weak red emission is mainly caused by energy transfer up–conversion (ETU) process. In this study, the red emission possesses highest intensity compared to the other two green emissions. The possible process involved in the up–converted emission for our glasses will be discussed with the aid of an energy level diagram (Fig. 11). First, the ground–state absorption (GSA) begins at 779 nm and excites electrons in the Er^{3+} ions to the metastable state at $^4I_{9/2}$, and then the electrons relax non–radiatively (NR) to the $^4I_{11/2}$ state by phonon relaxation. The electrons later absorb another 779 nm photon and re–excites to the state of $^4F_{3/2}$ via the ESA process. Electrons in this state NR decay to $^2H_{11/2}$, $^4S_{3/2}$ and $^4F_{9/2}$ levels followed by radiative relaxation to the ground state ($^4I_{15/2}$) to offer greens (518 and 556 nm) and red (647 nm) up–converted emissions, respectively. However, due to the wide gap between the $^4S_{3/2}$ and $^4F_{9/2}$ levels (~2800 cm^{-1}), the probability of populating $^4F_{9/2}$ by multi–phonon relaxation is small giving only a weak red emission. As such, the red emission requires an increase in the population of the $^4F_{9/2}$ by energy transfer (ET) from V^{4+} to the Er^{3+} ions which result in the large enhancement of 647 nm peak. The ET fromV^{4+} to Er^{3+} was mainly through two ways; one way is from the relaxed level V^{4+}:$^2B_2$ to the Er^{3+}:$^4F_{9/2}$ through resonant ET. The other way is due to the similar matching energy separation between the two levels, V^{4+} transfer its energy to Er^{3+} via $^2B_1(V^{4+}) + {}^4I_{15/2}(Er^{3+}) \rightarrow {}^2B_2(V^{4+}) + {}^4F_{9/2}(Er^{3+})$ for the population of $^4F_{9/2}$ level and subsequently strong red emission. The energy level scheme of V_2O_5 consisting of an absorption band at 16,900 cm^{-1} (inset Fig. 5) signifies shows the ET between V^{4+} and Er^{3+} in the visible the electronic distribution of V^{4+} ($^2B_1 \leftrightarrow {}^2B_2$).

Additional evidence of ET is obtained by determining the decay time of the luminescence from a donor. As shown in Fig. 12, the obtained PL decay curves do not follow single exponential decay which verified the ET process from V^{4+} to Er^{3+} ions. Faster decay and decrement in τ_{exp} of V^{4+} emission with surge in Er^{3+} concentration may be due to the effective ET from sensitizer V^{4+} to activator Er^{3+} ions in co–doped Na_2O–CaO–B_2O_3 glasses. The considerable close distance between Er^{3+} and V^{4+} promotes ET where narrow energy level between state foster multiphoton relaxation (MP). The decrease in τ_{exp} in presence of V^{4+} ions could be related to the non-radiative ET from V^{4+} to Er^{3+} ions and is also validates the result obtained from the photoluminescence spectra given in Fig. 10 (a). From the result, the addition of V^{4+} ions help in enhancing the Er^{3+} intensity of red emission.

The effect of V_2O_5 co–doping in the Er^{3+} –doped glasses on visible emission spectra was investigated by fixing the concentration of Er_2O_3 in Series A glasses. The highest band intensities for all transitions observed at $x = 0.5$ mol% [Fig. 10 (c)] can be interpreted due to influence of asymmetry around Er^{3+} ion sites as the computed oscillator strength (f_{exp}) and Ω_2 [Fig. 8 (a)] which showed highest value at $x = 0.5$ mol%. This indicates strongest site asymmetry for $x = 0.5$ mol% among samples which induces strong local electric field near Er^{3+} ions, causing enhanced emissions. The highest PL intensities is also benefited from the enhancement of structure rigidity corresponded to the increase in Ω_4 and Ω_6 [inset Fig. 8 (a)]. On the contrary, the PL intensities minimum observed at $x = 1.5$ mol% was not accompanied by f_{exp} minimum, suggesting that asymmetry surrounding Er^{3+} may not contribute to the drop in PL intensity, but exhibits quite similar trend to DC conductivity where a minimum observed at $x = 1.5$ mol% for Er_2O_3–free $20Na_2O$–$20CaO$–$(60 - x)B_2O_3$:xV_2O_5 glass system [7]. As such, the minimum in PL at $x = 1.5$ mol% is suggested due to the MIE effect. Although, the mechanism of the effect is not clear, it may involve changing roles of V_2O_5 from network former ($x < 1.5$ mol%) to network modifier ($x \geq 1.5$ mol%), as revealed by FTIR results. The decrease in PL intensities for $0.5 < x \leq 1.5$ mol% may be attributed to V_2O_5 occupying network forming position with VO_5 groups, where V_2O_5 forms strong

V–O covalent bond and electrons were more tied up in bond formation. However, for $x \geq 1.5$ mol%, V_2O_5 acts as glass modifier, the oxygens break the local symmetry of the glass network converting VO_5 tbp into VO_4 polyhedral groups while V^{4+} ions occupy interstitial positions [69, 70]. The interstitial V^{4+} ions are suggested to be involved in energy transfer to Er^{3+} energy level leading to the increase in PL intensities for $x \geq 1.5$ mol% [Fig. 10 (c)].

Meanwhile, the up–converted PL spectra for the glass in Series B [Fig. 10 (b)] exhibited different effects of Er^{3+} ion concentration on the glass system. The increased intensity of emission band at $y = 2.0$ mol% indicating a high emission efficiency and a decreased intensity for $y = 3.0$ mol% Er_2O_3 indicating a low emission efficiency. Although it can be observed that Ω_2 decreases [inset Fig. 8 (b)], there is largest enhancement in PL from $y = 1.0$ mol% to $y = 2.0$ mol% showing a possibility of an increased amount of Er^{3+} emitters with increasing Er_2O_3. The result of parameter Ω_6 showed slightly increases at $y = 2.0$ mol% before declined at $y = 3.0$ mol% [inset Fig. 8 (b)] certainly serve to reinforce the key idea of increasing Er^{3+} ionicity induced electric dipole transition hence the observed highly efficient PL at $y = 2.0$ mol% [71]. PL intensity is commonly expected to decrease in less rigid glass matrix, the increased of Er^{3+} ion concentrations in this glass system and reducing Er^{3+} covalency seems to play a dominant role that leads to largest PL enhancement for sample $y = 2.0$ mol%. As such, this points out that the bulk rigidity of glasses has less influence in the PL emission. On the other hand, the smaller Ω_4 and larger Ω_6 values observed for the glass sample is favorable for the emission transition, as reported previously [40]. However, further substitution of Er_2O_3 at $y = 3.0$ mol% caused the emission intensity to diminish probably due to a clustering effect, as discussed earlier. Concentration quenching amongst clustered RE ions is well known to result in decreased PL intensity [61]. This reduction occurs through the cross–relaxation process, where energy transfer takes placed from the excited state of the Er^{3+} ion to the neighboring Er^{3+} ions lying in the ground state. The lower PL intensity of sample contain 2.0 mol% Er_2O_3 in Series B than PL intensity obtained for sample $x = 1.5$ mol% V_2O_5 indicates that optimum PL of Er^{3+}/V^{4+} co–doped Na_2O–CaO–B_2O_3 glasses depends critically on glass host rather than activator concentration.

5. Conclusion

The effects of Er^{3+}/V^{4+} ions co–doping on optical absorption and PL spectra of Er_2O_3 in MIE Na_2O–CaO–B_2O_3–V_2O_5 glasses were investigated. For Series A, both oscillator strength (f_{exp}) and Judd–Ofelt parameters ($\Omega_{2,4,6}$) increased to a maximum value at $x = 0.5$ mol% V_2O_5 in which was attributed to structural changes induced by V_2O_5 participating in the host glass matrix as revealed by FTIR and ultrasonic investigations. PL maximum coincided with f_{exp} maximum at the same position and is suggested to be related to the enhancement in the absorption, whereas anomalous PL intensity at $x = 1.5$ mol% reveals the presence of the influence of MIE effect on emission. However, the MIE effect does not manifest in the f_{exp} and all Judd–Ofelt parameters. For Series B, the drop in PL for sample $x = 1.5$ mol% V_2O_5 have been compensated by addition of Er^{3+} ions until $y = 2.0$ mol% Er_2O_3 before luminescence quenching take place at $y = 3.0$ mol% as a result of formation of Er^{3+} ion clustering. Based on energy level diagram, three up–converted PL bands at 518, 556 and 647 nm under 779 nm excitation were attributed to emission transition of Er^{3+} ion from $^2H_{11/2}$, $^4S_{3/2}$ and $^4F_{9/2}$ to $^4I_{15/2}$ ground state, respectively. The relaxation of the populated $^4F_{9/2}$ to the ground state which responsible for strong red emission (647 nm) is suggested not only by excited state absorption process followed by three–step non–radiative decay process but assisted with energy transfer from $^2B_1 \rightarrow {}^2B_2$ transition of V^{4+} to the Er^{3+} ions.

Credit author statement

The specific contributions made by each author is indicated here: Conception and design of study: S. N. Mohamed, A. K. Yahya. Supervised the research: A. K. Yahya. Verified the methods: S.N. Mohamed, E. S. Sazali. Acquisition of data: S. N. Mohamed, E. S. Sazali. Analysis and/or interpretation of results: S. N. Mohamed, E. S. Sazali, A. K. Yahya.

Declaration of competing interest

The authors declare that they have no known competing financial interests or personal relationships that could have appeared to influence the work reported in this paper.

Acknowledgement

This project was financially supported by the Ministry of Higher Education Malaysia under the research FRGS grant [600–IRMI/FRGS 5/3 (038/2019)]. The authors would like to express gratitude to Research Management Center, Universiti Teknologi Mara for assistance throughout the research. Moreover, S. N. Mohamed would like to thank the Universiti Teknologi Mara and the Ministry of Education of Malaysia for providing the SLAB scholarship.

References

[1] R. El–Mallawany, M.D. Abdalla, I.A. Ahmed, New tellurite glass: optical properties, Mater. Chem. Phys. 109 (2008) 291–296.
[2] S.K. Arya, G. Kaur, K. Singh, Effect of vanadium on the optical and physical properties of lithium borate glasses, J. Non-Cryst. Solids 432 (2015) 393–398.
[3] S.J. Japari, A.K. Yahya, R. Hisam, Effects of mixed–alkali oxides on AC conductivity and dielectric properties of xNa$_2$O–(20 –x)K$_2$O–30V$_2$O$_5$–50TeO$_2$ glasses, Results Phys. 16 (2020), 102905.
[4] R. Hisam, A.K. Yahya, H.M. Kamari, Z.A. Talib, AC conductivity and dielectric behavior in mixed electronic–ionic 30Li$_2$O–4MoO$_3$–(66 –x)TeO$_2$–xV$_2$O$_5$ glass system, Ionics 23 (6) (2017) 1423–1427.
[5] J.E. Garbarczyk, M. Wasiucionek, P. Jóźwiak, L. Tykarski, J.L. Nowiński, Studies of Li$_2$O–V$_2$O$_5$–P$_2$O$_5$ glasses by DSC, EPR and impedance spectroscopy, Solid State Ionics 154 (2002) 367–373.
[6] E. Mansour, K. El–Egili, G. El–Damrawi, Ionic–polaronic behavior in CeO$_2$–PbO–B$_2$O$_3$ glasses, Phys. B Condens. Matter 392 (2007) 221–228.
[7] S.N. Mohamed, A.K. Yahya, Effects of V$_2$O$_5$ on elastic, structural, and optical properties of mixed ionic–electronic 20Na$_2$O–20CaO–(60 –x)B$_2$O$_3$–xV$_2$O$_5$ glasses, Ionics 24 (9) (2018) 2647–2664.
[8] L.S. Rao, M.S. Reddy, M.R. Reddy, N. Veeraiah, Dielectric dispersion in Li$_2$O–MoO$_3$–B$_2$O$_3$ glass system doped with V$_2$O$_5$, J. Alloys Compd. 464 (2008) 472–482.
[9] L. Murawski, R.J. Barczyński, D. Samatowicz, Electronic conductivity in Na$_2$O–FeO–P$_2$O$_5$ glasses, Solid State Ionics 157 (2003) 293–298.
[10] M.R. Dousti, R.J. Amjad, Z.A.S. Mahraz, Enhanced green and red upconversion emissions in Er^{3+}–doped boro–tellurite glass containing gold nanoparticles, J. Mol. Struct. 1079 (2015) 347–352.
[11] N. Effendy, S.H.A. Aziz, H.M. Kamari, K.A. Matori, M.H.M. Zaid, Enhanced green photoluminescence of erbium doped Zn$_2$SiO$_4$ glass–ceramics as phosphor in optoelectronic devices, J. Alloys Compd. 783 (2019) 441–447.
[12] F.L. Zhang, H. Hu, Lin, Emission properties of highly doped Er^{3+} fluoroaluminate glass, Mater. Lett. 47 (2001) 189.
[13] Z.A. Said Mahraz, M.R. Sahar, S.K. Ghoshal, M. Reza Dousti, Concentration dependent luminescence quenching of Er^{3+}–doped zinc boro–tellurite glass, J. Lumin. 144 (2013) 139–145.
[14] G. Tang, et al., Efficient 2.0 m emission in Er^{3+}/Ho^{3+} co–doped barium gallo–germanate glasses under different excitations for mid–infrared laser, J. Alloys Compd. 664 (19–24) (2016).
[15] Q. Zhang, G.R. Chen, G. Zhang, J.R. Qiu, D.P. Chen, Spectroscopic properties of Ho^{3+}/Yb^{3+} codoped lanthanum aluminum germanate glasses with efficient energy transfer, J. Appl. Phys. 106 (2009), 113102.
[16] Y. Gandhi, I.V. Kityk, M.G. Brik, P.R. Rao, N. Veeraiah, Influence of tungsten on the emission features of Nd^{3+}, Sm^{3+} and Eu^{3+} ions in ZnF$_2$–WO$_3$–TeO$_2$ glasses, J. Alloys Compd. 508 (2010) 278–291.
[17] K. Neeraja, T.G.V.M. Rao, A. Rupesh Kumar, N. Veeraiah, M. Rami Reddy, Influence of modifier oxide on Spectroscopic properties of Ho^{3+}: V^{4+} co–doped Na$_2$O–SiO$_2$–ZrO$_2$ glasses, J. Alloys Compd. 586 (2014) 159–168.
[18] C. Venkateswarlu, M. Seshadri, Y.C. Ratnakaram, Influence of mixed alkalis on spectroscopic parameters of Sm^{3+}, Dy^{3+} doped chloroborate glasses, Opt. Mater. 33 (2011) 799–806.
[19] N.B. Mohamed, A.K. Yahya, M.S.M. Deni, S.N. Mohamed, M.K. Halimah, H.A. A. Sidek, Effects of concurrent TeO$_2$ reduction and ZnO addition on elastic and structural properties of (90–x)TeO$_2$–10Nb$_2$O$_5$–(x)ZnO glass, J. Non-Cryst. Solids 356 (2010) 1626–1630.
[20] I. Jlassi, N. Sdiri, H. Elhouichet, M. Ferid, Raman and impedance spectroscopy methods of P$_2$O$_5$–Li$_2$O–Al$_2$O$_3$ glass system doped with MgO, J. Alloys Compd. 645 (Oct. 2015) 125–130.

[21] F. Ciorcas, S.K. Mendiratta, I. Ardelean, M.A. Valente, Structural and magnetic studies of CuO–TeO_2 and CuO–TeO_2 –B_2O_3 glasses, Eur. Phys. J. B 20 (2001) 235–240.

[22] S.A. Salehizadeh, B.M.G. Melo, F.N.A. Freire, M.A. Valente, M.P.F. Graça, Structural and electrical properties of TeO2–V2O5–K2O glassy systems, J. Non-Cryst. Solids 443 (2016) 65–74.

[23] M.H.M. Zaid, et al., Comprehensive study on compositional dependence of optical band gap in zinc soda lime silica glass system for optoelectronic applications, J. Non-Cryst. Solids 449 (2016) 107–112.

[24] A. Edukondalu, B. Kavitha, M.A. Samee, S.K. Ahmmed, S. Rahman, K.S. Kumar, Mixed alkali tungsten borate glasses – optical and structural properties, J. Alloys Compd. 552 (2013) 157–165.

[25] N.S. Sabri, A.K. Yahya, R. Abd–Shukor, M.K. Talari, Anomalous elastic behaviour of xSrO–10PbO–(90–x)B_2O_3 glass system, J. Non-Cryst. Solids 444 (2016) 55–63.

[26] S. Laila, S.N. Supardan, A.K. Yahya, Effect of ZnO addition and concurrent reduction of V_2O_5 on network formation and elastic properties of lead vanadate (55−x)V_2O_5–45PbO–(x)ZnO glass system, J. Non-Cryst. Solids 367 (2013) 14–22.

[27] R.N. Bhargava, R.A. Condrate, The vibrational spectra of VPO_5 crystal phases and related glasses, Appl. Spectrosc. 31 (3) (1977) 230–236.

[28] Y. Dimitriev, V. Dimitrov, M. Arnaudov, Infra-red spectra of crystalline phases and related glasses in the TeO_2-V_2O_5-Me_2O system, J. Mater. Sci. 14 (3) (1979) 723–727.

[29] E. Mansour, Structure and electrical conductivity of new Li2O–CeO2–B2O3 glasses, J. Non-Cryst. Solids 357 (2011) 1364–1369.

[31] K. Annapoorani, C. Basavapoornima, N. Suriya Murthy, K. Marimuthu, Investigations on structural and luminescence behavior of Er^{3+} doped Lithium Zinc borate glasses for lasers and optical amplifier applications, J. Non-Cryst. Solids 447 (2016) 273–282.

[32] E.S. Sazali, R. Sahar, S.K. Ghoshal, S. Rohani, R. Arifin, Judd-ofelt intensity parameters of erbium doped lead tellurite glass, Journal of Non-Oxide Glasses 6 (2014) 61–67.

[33] E.S. Sazali, M.R. Sahar, S.K. Ghoshal, R. Arifin, M.S. Rohani, A. Awang, Optical properties of gold nanoparticle embedded Er^{3+} doped lead–tellurite glasses, J. Alloys Compd. 607 (2014) 85–90.

[34] S.M. Saheb, R. Vijay, P.R. Babu, G.N. Raju, Structural and spectroscopic studies on lead germanate glasses doped with V_2O_5, in: Mater. Today Proc. 5, Elsevier, 2018, pp. 26304–26313.

[37] R. El–Mallawany, Tellurite glasses: Part 1. Elastic properties, Mater. Chem. Phys. 53 (2) (1998) 93–120.

[38] S.P. Sinha, Complexes of the Rare Earths, Pergamon Press, Oxford, UK, 1966.

[39] J. Anjaiah, C. Laxmikanth, N. Veeraiah, Spectroscopic properties and luminescence behaviour of europium doped lithium borate glasses, Phys. B Condens. Matter 454 (2014) 148–156.

[40] E.S. Sazali, M.R. Sahar, S.K. Ghoshal, R. Arifin, M.S. Rohani, R.J. Amjad, Efficient optical enhancement of Er^{3+} doped lead–tellurite glass embedded with gold nanoparticles: role of heat–treatment, J. Non-Cryst. Solids 410 (2015) 174–179.

[41] G. Lakshminarayana, H. Yang, J. Qiu, Photoluminescence of Pr^{3+}–, Nd^{3+}– and Ni^{2+}– doped TeO_2–ZnO–WO_3–TiO_2–Na_2O glasses, J. Alloys Compd. 475 (2009) 569–576.

[42] C.J. Ballhausen, H.B. Gray, The electronic structure of the vanadyl ion, Inorg. Chem. 1 (1962) 111–122.

[43] F.H. Margha, M.A. Marzouk, Influence of vanadium addition on the optical and photoluminescence properties of borate glasses and their glass – ceramic derivatives, Appl. Phys. A 5 (2019) 1–9.

[44] R. Slama, F. Ghribi, A. Houas, C. Barthou, L. El Mir, Visible photocatalytic properties of vanadium doped zinc oxide aerogel nanopowder, Thin Solid Films 519 (2011) 5792–5795.

[45] L. Li, Z. Zhou, H. Tian, D. Gong, Z. Yang, Y. Yang, Spectroscopic and upconversion properties of erbium-doped potassium lithium tantalate niobate crystals under 800 nm femtosecond laser excitation, J. Appl. Phys. 108 (2010), 043520.

[46] H. Doweidar, G.M. El–Damrawi, Y.M. Moustafa, R.M. Ramadan, Density of mixed alkali borate glasses: a structural analysis, Phys. B Condens. Matter 362 (2005) 123–132.

[47] M. Bosca, L. Pop, G. Borodi, P. Pascuta, E. Culea, XRD and FTIR structural investigations of erbium–doped bismuth–lead–silver glasses and glass ceramics, J. Alloys Compd. 479 (2009) 579–582.

[48] M.H.A. Mhareb, et al., Optical and erbium ion concentration correlation in lithium magnesium borate glass, Optik 126 (2015) 3638–3643.

[49] K. Neeraja, T.G.V.M. Rao, A.R. Kumar, V. Uma Lakshmi, N. Veeraiah, M. Rami Reddy, Spectroscopic properties of Sm^{3+} and V^{4+} ions in Na_2O–SiO_2–ZrO_2 glasses, J. Mol. Struct. 1054–1055 (2013) 339–348.

[50] X. Wei, L. Jiao, S. Liu, J. Sun, W. Peng, H. Gao, H. Yuan, Synthesis and electrochemical performance of V_2O_5 doped MoO_3 cathode materials, Journal. Alloys Compd. 486 (2009) 672–676.

[51] G. Upender, S. Ramesh, M. Prasad, V.G. Sathe, V.C. Mouli, Optical band gap, glass transition temperature and structural studies of (100−2x)TeO_2–xAg_2O–xWO_3 glass system, J. Alloys Compd. 504 (2010) 468–474.

[52] E.A. Mohamed, F. Ahmad, K.A. Aly, Effect of lithium addition on thermal and optical properties of zinc–tellurite glass, J. Alloys Compd. 538 (2012) 230–236.

[53] D. Souri, S.A. Salehizadeh, Effect of NiO content on the optical band gap refractive index, and density of TeO_2–V_2O_5–NiO glasses, J. Mater. Sci. 144 (2009) 5800–5805.

[54] M.M. Umair, A.K. Yahya, M.K. Halimah, H.A.A. Sidek, Effects of increasing tungsten on structural, elastic and optical properties of $x$$WO_3$–(40 –x) Ag_2O–60Te_2O glass system, J. Mater. Sci. Technol. 31 (2015) 83–90.

[55] V. Kamalaker, G. Upender, C. Ramesh, V. Chandra Mouli, Raman spectroscopy, thermal and optical properties of TeO_2–ZnO–Nb_2O_5–Nd_2O_3 glasses, Spectrochim. Acta Part A Mol. Biomol. Spectrosc. 89 (2012) 149–154.

[56] Y.B. Saddeek, I.S. Yahia, K.A. Aly, W. Dobrowolski, Spectroscopic, mechanical and magnetic characterization of some bismuth borate glasses containing gadolinium ions, Solid State Sci. 12 (2010) 1426–1434.

[57] W.B. Fowler, D.L. Dexter, Relation between absorption and emission probabilities in luminescent centers in ionic solids, Phys. Rev. 128 (1962) 2154–2165.

[58] M. Vijayakumar, K. Marimuthu, Structural and luminescence properties of Dy^{3+} doped oxyfluoro–borophosphate glasses for lasing materials and white LEDs, J. Alloys Compd. 629 (2015) 230–241.

[59] M.B. Saisudha, J Ramakrishna, Effect of host glass on the optical absorption properties of Nd^{3+}, Sm^{3+}, and Dy^{3+} in lead borate glasses, Phys. Rev. B Condens. Matter 53 (1996) 6186–6196.

[60] J. Yang, S. Dai, Y. Zhou, L. Wen, L. Hu, Z. Jiang, Spectroscopic properties and thermal stability of erbium–doped bismuth–based glass for optical amplifier, J. Appl. Phys. 93 (2003) 977–983.

[61] S.W. Yung, et al., Thermal, chemical, optical properties and structure of Er^{3+}–doped and Er^{3+}/Yb^{3+}–codoped P_2O_5–Al_2O_3–ZnO glasses, J. Non-Cryst. Solids 357 (2011) 1328–1334.

[62] S. Hraiech, C. Bouzidi, M. Férid, Luminescence properties of Er^{3+}–doped phosphate glasses, Phys. B Condens. Matter 522 (2017) 15–21.

[63] S.Y. Moustafa, M.R. Sahar, S.K. Ghoshal, Erbium ions oscillator strength and emission enhancement in antimony phosphate amorphous matrix, J. Non-Cryst. Solids 433 (2016) 87–94.

[64] F. Auzel, f–f, Oscillator strengths, hypersensitivity, branching ratios and quantum efficiencies discussed in the light of forgotten results, J. Alloys Compd. 380 (2004) 9–14.

[65] Y.C. Ratnakaram, D.T. Naidu, A. Vijayakumar, J.L. Rao, Studies on optical absorption and luminescence properties of Dy^{3+} doped mixed alkali borate glasses, Opt. Mater. 27 (2004) 409–417.

[66] I. Pal, A. Agarwal, S. Sanghi, M.P. Aggarwal, Spectroscopic and radiative properties of Nd^{3+} ions doped zinc bismuth borate glasses, Indian J. Pure Appl. Phys. 51 (2013) 18–25.

[68] A. Mardhiah, K. Azman, H. Azhan, W.A.W. Razali, Optical characterization of erbium doped sodium borate glass, Adv. Mater. Res. 622–623 (2012) 191–194.

[69] A. Ghosh, S. Bhattacharya, A. Ghosh, Optical and other structural properties of some zinc vanadate semiconducting glasses 490 (2010) 480–483.

[70] K. Srilatha, et al., The role of vanadium valence states and coordination on electrical conduction in lithium iodide borate glasses mixed with small concentration of silver iodide, J. Non-Cryst. Solids 357 (2011) 3538–3547.

[71] H.B. Poor, H.A. Aziz, R. Zamiri, Ultrasonic and optical properties and emission of Er^{3+}/Yb^{3+} doped lead bismuth–germanate glass affected by Bi^{+}/Bi^{2+} ions, J. Lumin. 143 (2013) 526–533.